Originally published as:

# Hot subduction in the middle Jurassic and partial melting of oceanic crust in Chilean Patagonia

Samuel Angiboust[1,2*]

Thais Hyppolito[3,4]

Johannes Glodny[1]

Aitor Cambeses[4]

Antonio Garcia-Casco[4,5]

Mauricio Calderón[6]

Caetano Juliani[3]


1: GFZ German Research Centre for Geosciences, 14473 Potsdam, Germany (*: _corresponding author_; angiboust@ipgp.fr ; glodnyj@gfz-potsdam.de)

2: Institut de Physique du Globe de Paris, Sorbonne Paris Cité, Univ. Paris Diderot, CNRS, F-75005 Paris, France

3: Instituto de Geociências, Rua do Lago, 562, Universidade de São Paulo, 05505-080, São Paulo, Brazil (thahyppolito@gmail.com)

4: Facultad de Ciencias, Universidad de Granada, Fuentenueva s/n 18071, Granada, Spain (agcasco@ugr.es and aitorc@ugr.es)

5: Andalusian Institute of Earth Sciences, CSIC-Univ. Granada, Spain

6: Carrera de Geología,  Universidad Andres Bello, Sazie 2119,  Santiago, Chile. (mccaldera@gmail.com)

**ABSTRACT**

1  Rare remnants of a Mesozoic subduction high pressure (HP) accretionary complex

2  are exposed on Diego de Almagro Island in Chilean Patagonia. We herein focus on

3  the Lazaro unit, a coherent slice of oceanic crust exposed on this island that has

4  been first affected by high temperature (HT) metamorphism followed by a lower

5  temperature deformation event (LT). Its Pressure-Temperature-time (P-T-t) evolution

6  is reconstructed using field and petrographic observations, phase relations,

7  thermobarometry and geochronology. Remnants of a primary amphibolite to HP

8  granulite-facies event in mafic rocks comprising garnet (with ilmenite exsolutions),

9  diopside, trondhjemitic melt, pargasite, plagioclase ± epidote are reported for the first

10  time in neosomes, indicating peak P-T conditions of 1.1-1.3 GPa and c. 750°C. This

11  peak T paragenesis has been thoroughly overprinted by a phengite-chlorite-actinolite

12  assemblage during isobaric cooling down to c. 450°C. U-Pb dating of zircon

13  metamorphic rims from a metasedimentary rock yielded a homogeneous age

14  population of 162 ± 2 Ma for the HT event. Sm-Nd dating of two peritectic garnet-

15  bearing samples yield ages of 163 ± 2 Ma and 163 ± 18 Ma for the HT event. Multi-

16  mineral Rb-Sr dating of a metasedimentary rock overprinted by LT deformation

17  suggests retrograde shearing between 120 and 80 Ma. Our results show that the HT

18  event in the Lazaro unit took place at around 160-165 Ma, shortly before the onset of

19  Patagonian Batholith emplacement. Partial melting of subducted oceanic crust

20  reported in the Lazaro unit is related to the early stages of hot subduction along the

21  Gondwana western margin. The Lazaro unit remained at c. 40 km depth along the

22  subduction interface for more than 80 Ma, recording the deformation and long-term

23  cooling of the subduction channel environment until the upper Cretaceous.

## 1. INTRODUCTION

During the consumption of oceanic lithosphere, fluids and melts from the lower plate are transferred to the upper plate, leading to partial melting of the ultramafic wedge and the formation of volcanic arcs, ultimately contributing to the chemical differentiation of the Earth (Tatsumi and Eggins, 1995). Mass transfer processes across the subduction interface have been extensively studied via geochemical, petrological and geophysical investigations (Peacock et al., 1994; Oncken et al., 2003; Maruyama et al., 2009; Spandler and Pirard, 2013; Schmidt and Poli, 2014). Although subject to contamination during migration through the upper plate, arc magmas and volcanic rocks yield valuable information on chemical differentiation and volatile transport highlighting the contribution of various lithological compounds to the melting process (e.g. Plank and Langmuir, 1993; Walowski et al., 2015). Furthermore, high pressure rocks and exhumed former subduction interfaces have the potential to provide *in situ* insights into natural processes taking place within the mantle wedge region and beneath volcanic arcs (e.g. Hermann et al., 2006; John et al., 2012).

Only a few natural examples documenting partial melting processes and trondhjemite-tonalite genesis in oceanic subduction zones have been reported (e.g. Catalina Schists: Sorensen and Barton, 1987; Cuba mélanges: Garcia-Casco et al., 2008, Lazaro and Garcia-Casco, 2008; N. Iran: Rossetti et al., 2010). The apparent

48   scarcity of such occurrences can be explained by the rarity of material exhumed from

49   sub-arc depths (>100 km) where temperatures are high enough (>700°C) to enable

50   partial melting of the oceanic crust along normal subduction gradients (e.g. Syracuse

51   et al., 2010). Known occurrences of melt-bearing, exhumed oceanic crust localities

52   correspond to shallower rocks subducted along a hot prograde pressure-temperature

53   (P-T) path (c. 20°/km). Such conditions may have been reached (i) during Archean

54   times (e.g. van Hunen and Moyen, 2012), (ii) shortly after subduction initiation (e.g.

55   Stern et al., 2004) or (iii) during subduction of young oceanic lithosphere (e.g.

56   Blanco-Quintero et al., 2011).

57   We herein report a new occurrence of high-pressure partial melting of

58   subducted oceanic crust on the remote Diego de Almagro Island (**Fig.1**; DAI, Chilean

59   Patagonia) and discuss the meaning of this event in the light of new

60   thermobarometric, geochemical and geochronological data. This island represents a

61   unique vestige of a fossil accretionary system developed at the southwestern margin

62   of Gondwana (Hervé and Fanning, 2003; Willner et al., 2004), where different slices

63   of oceanic crust were underplated between c. 120 Ma and c. 80 Ma and

64   metamorphosed under blueschist to eclogite-facies conditions (Hyppolito et al.,

65   2016). The new results presented here open a window for better understanding the

66   origin of partially molten rocks in this paleo-subduction system and their tectonic

67   significance in a regional context.
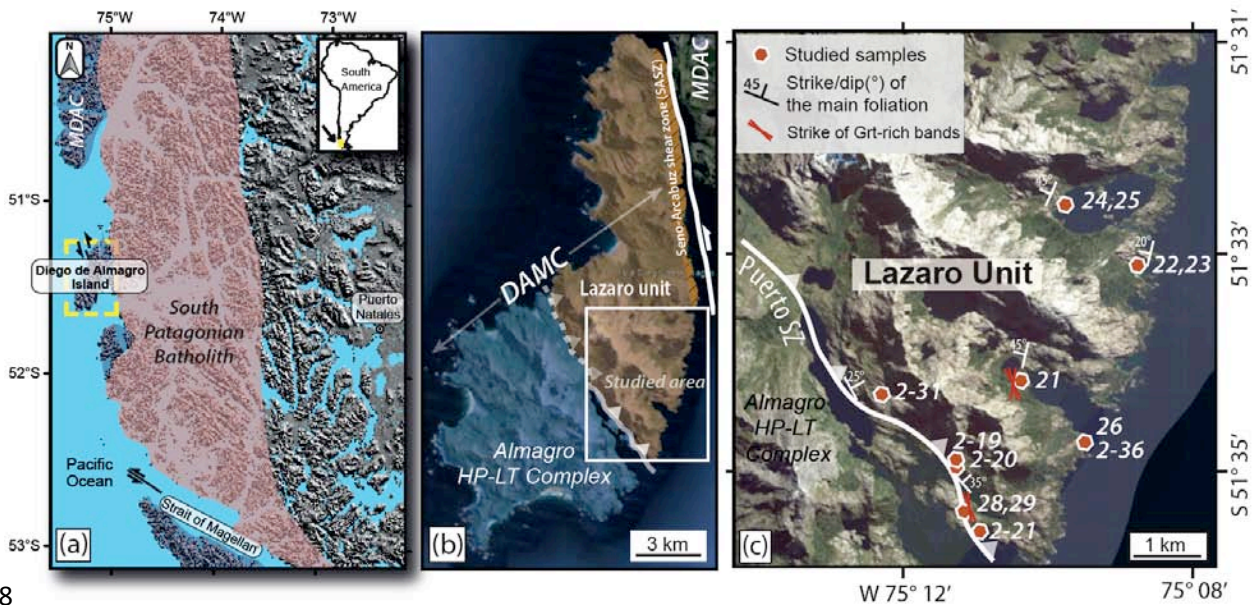
**Figure 1:** Geological map of the Lazaro unit. **a**. Location of Diego de Almagro Island in Chilean Patagonia. **b**. Simplified geological map of the island showing the main units forming the Diego de Almagro Metamorphic Complex (DAMC) and the Seno Arcabuz Shear Zone (SASZ) that partly reworked the structure in the Lazaro unit (MDAC: Madre de Dios Accretionary Complex). **c**. Satellite image showing the sampling localities as well as the main structural features.

## 2. GEOLOGICAL SETTING

A very lengthy mountain chain, the Chilean Coastal Cordillera, is exposed almost continuously between latitudes 28º S and 55º S, and includes subduction complexes of Late Paleozoic and Mesozoic ages developed at the southwestern margin of the Gondwana continent via basal and frontal accretionary processes (Hervé, 1988; Glodny et al., 2005; Willner, 2005; Kato and Godoy, 2015). Only three occurrences of albite-epidote amphibolite-facies subduction channel rocks (with counter-clockwise P-T paths) have been described along these coastal complexes (Los Pabilos: Willner et al., 2004b; Kato et al., 2008; Punta Sirena: Willner et al., 2005; Hyppolito et al., 2014; Los Caldos: Willner et al., 2012). South of ca. 46° S, on

5

the western side of the South Patagonian Batholith, isolated exposures of Mesozoic accretionary complexes occur (e.g. Madre de Díos, Diego de Almagro and Diego Ramirez complexes) (e.g. Hervé et al., 2008). Diego de Almagro Island (DAI) is a remote locality (51° 30' S) close to the Strait of Magellan in Chilean Patagonia (**Fig.1a**), which embraces outcrops of Mesozoic metamorphic complexes formed during subduction of the paleo-Pacific ocean beneath the western margin of Gondwana (e.g. Charrier et al., 2007; Hervé et al., 2007; Willner et al., 2004a). To the East of the DAI is exposed the Madre de Díos Accretionary Complex (MDAC), a frontally accreted Triassic actinolite-pumpellyite-facies accretionary prism (Forsythe and Mpodozis, 1979; Hervé et al., 1999; Sepúlveda et al., 2010) where peak metamorphic conditions of ~290–310 °C and 0.4-0.6 GPa have been determined (Willner et al., 2009; **Fig.1a**). The DAI is formed by the Cretaceous accretionary Diego de Almagro Metamorphic Complex (DAMC) (Hervé and Fanning, 2003; Willner et al., 2004a; Hyppolito et al., 2016). The MDAC and DAMC, which formed by diachronic tectonic processes, are now separated by a ductile NNW-trending shear zone (the Seno Arcabuz Shear zone: SASZ; Hervé and Fanning; Olivares et al., 2003; Willner et al., 2004; 2009). Sinistral strike-slip transport along this shear zone led to partial reworking of the eastern part of the DAI and juxtaposition of the MDAC (**Fig.1b**; e.g. Hervé et al., 1999; Olivares et al., 2003; Willner et al., 2009). The main amphibolite-facies deformation event along the SASZ has been estimated from orthogneisses by Willner et al. (2004a) to be around 580-690°C and 0.5-0.6 GPa. A K-Ar analysis of muscovite yielded an age of 122 ± 4.6 Ma for a garnet mica schist from the SASZ. Willner et al. (2004a) interpreted the HT metamorphism of the SASZ as a consequence of heat advection from the coeval magmatic arc suggesting the formation of a paired belt system in the DAMC (coeval HP-LT and LP-HT belts).

Some DAMC rocks have revealed mid- to late Jurassic protoliths metamorphosed during the early Cretaceous (Hervé et al., 1999; Hervé and Fanning 2003; Olivares et al., 2003; Willner et al., 2004a). Recent investigations (Hyppolito et al., 2016) have shown that the DAMC is divided into two main parts: the Almagro HP-LT Complex (AC) to the SW and the Lazaro unit to the NE. The Lazaro unit is limited to the E by the SASZ (**Fig.1c**). Both the Almagro HP-LT Complex (AC) and the Lazaro unit underwent HP metamorphism and are separated by a major, 50-100 m thick shear zone: the Puerto Shear Zone (PSZ; **Fig.1c**; Hervé and Fanning, 2003; Hyppolito et al., 2016). The AC is dominantly composed of N- and E-MORB-type mafic meta-tuffs and meta-pillow lavas with minor intercalations of metasediments (spessartine quartzites and pelitic schists) (Willner et al., 2004a; Hyppolito et al., 2016). Peak pressure metamorphic conditions have been estimated between 1.5 and 1.8 GPa (Hyppolito et al., 2016). Below the PSZ thrust, bodies with relics of eclogite-facies metamorphism with a strong amphibolite-facies overprint (the garnet amphibolite unit) yield multi-mineral Rb-Sr ages of c. 120 Ma (Hyppolito et al., 2016). The garnet amphibolite unit overlies (and is locally tectonically imbricated with) blueschist-facies rocks devoid of an amphibolite-facies overprint that yield much younger Rb-Sr deformation ages of c. 80 Ma (Hyppolito et al., 2016).

The Lazaro unit, on the other hand, has barely been investigated. A few orthogneiss samples have been studied by Hervé et al. (1999), Hervé and Fanning (2003) and Willner et al. (2004a). These authors noticed that some samples from the Lazaro unit rocks record metamorphism under a relatively warm thermal gradient and also proposed that an orthogneiss body exposed along the SASZ may represent a crustal fragment tectonically eroded from the upper plate that was juxtaposed with

7

135     HP-LT metamorphic rocks during subduction. The U-Pb age range of 165-170 Ma

136     obtained for zircon rims from a metagranite has been interpreted as a record of pre-

137     subduction extension-related magmatism associated with the break-off of Gondwana

138     during the late Jurasic (Hervé and Fanning, 2003), which culminated with the early

139     development of mafic oceanic-type crust (e.g. the Rocas Verdes basin) at c. 155 Ma

140     (Calderón et al., 2013).

141

142 **3.  3. ROCK TYPES AND FIELD RELATIONSHIPS OF THE LAZARO UNIT**

143         Two field missions focusing on the southern coast of the Diego de Almagro

144     Island were organized in 2007 and 2015. Sampling, petrological observations and

145     structural measurements led to the characterization of the Lazaro unit, a coherent

146     unit forming the eastern and south-eastern part of the island where abundant

147     amphibolite and orthogneiss bodies have been reported (Hervé and Fanning, 2003).

148     Our observations, in line with Hervé and Fanning (2003) and Willner et al. (2004a),

149     show that the Lazaro unit has been affected by an early pervasive HT tectono-

150     metamorphic stage followed by a LT overprint. The first HT metamorphic event led to

151     the formation of a subvertical metamorphic foliation striking N-S to NE-SW (**Fig.1c**;

152     **Electronic Appendix 1**). These primary structures are cross-cut by a series of NW-

153     SE striking, greenschist-facies shear zones sub-parallel to the main PSZ structure

154     (**Fig.1c**). High Temperature fabrics within the lowermost hundred meters of the

155     Lazaro unit have been transposed along the PSZ leading to the formation of C-S

156     greenschist-facies mylonites as well as rotation-recrystallization of garnet into

157     chlorite. Top-to-NW kinematic indicators as well as evidence of back-shearing have

158     been observed along this thrust contact, which dips 30° to the SE. Similar mylonites

159  are visible in the hanging wall of the underlying Almagro HP-LT Complex, which is

160  also affected by this mylonitization stage.
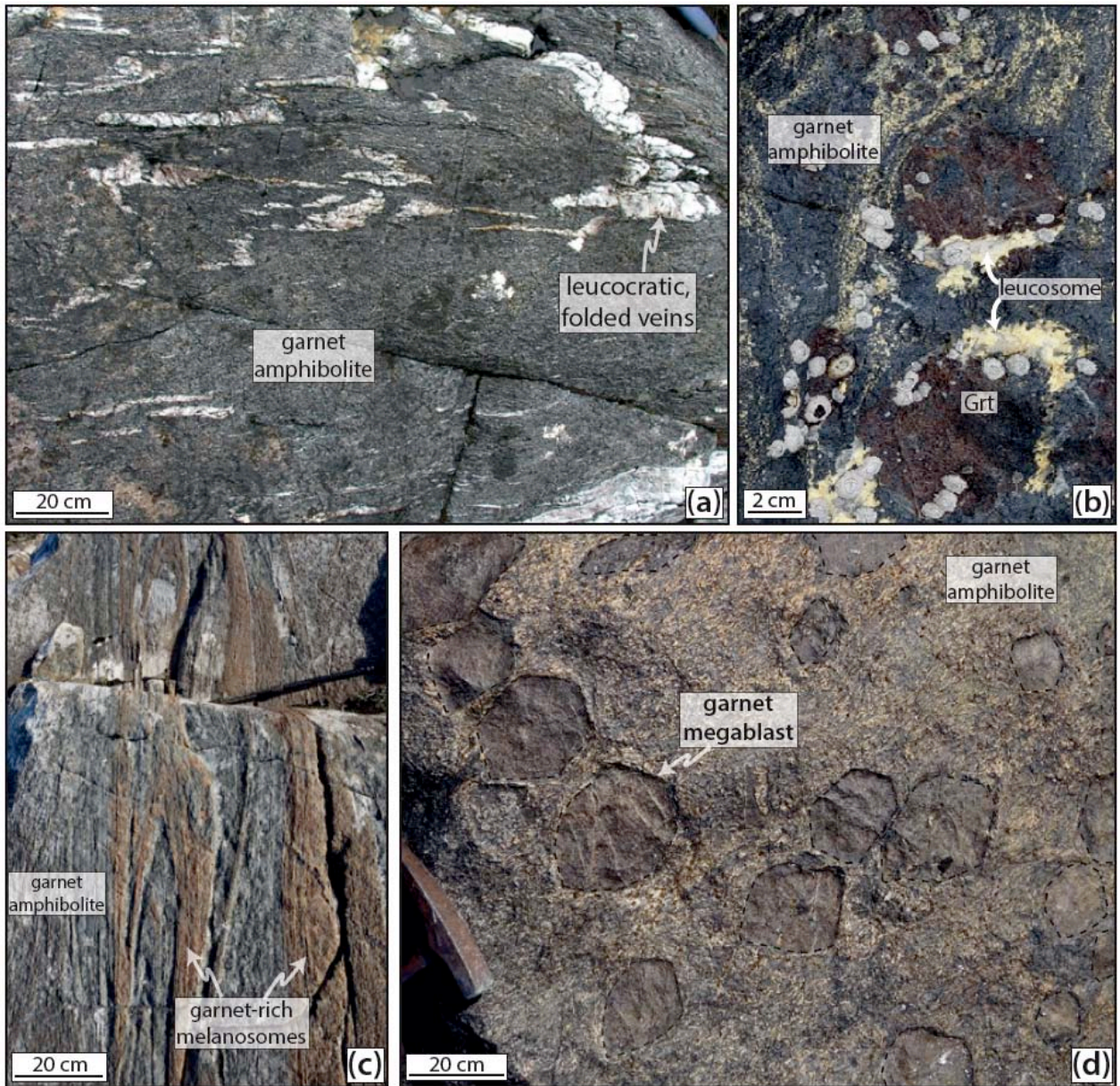
161



162  **Figure 2**: Field pictures of Lazaro unit exposures. **a**. Representative Lazaro unit outcrop

163  showing a dark, garnet amphibolite containing numerous decimeter-thick strongly folded

164  leucosomes. **b**. Coastal exposure of a garnet amphibolite (locality #25) showing 10-cm sized

165  peritectic garnet associated with a yellowish leucosome. **c**. Representative field view (locality

166  #29) of a garnet amphibolite matrix comprising garnetite layers that can continuously be

167  followed over hundreds of meters. **d**. Outcrop view of a garnet amphibolite (locality #26) in

168  which garnet megablasts of 15 to 25 cm in diameter can be observed (hammer for scale).

Evidence for an early high-temperature metamorphic event in the Lazaro unit is attested by the ubiquitous presence of garnet amphibolite and felsic gneiss in all sampling localities (**Fig.1c**; **Fig.2a and 2b**). The most frequent rock type in the studied area is a coarse-grained amphibolite with large amounts (> 50 vol.%) of dark amphibole crystals between 1 and 3 mm in size. At locality #21 (**Fig.1c**) a pluri-hectometric orthogneiss body occurs with coarse-grained intergrowths of hornblende crystals and fibrous epidote that exhibit a pegmatite-like structure (**Electronic Appendix 1**; see also Willner et al., 2004). At several localities (e.g #25 and #2-31), relics of a garnet-clinopyroxene-plagioclase assemblage suggest that peak metamorphic conditions reached the high pressure granulite facies of Pattison (2003) (stage 1; see **figure 3a**, and petrological results below). All studied localities also exhibit evidence of partial melting of amphibolite with two distinct types of neosomes (following the nomenclature of Sawyer, 2008). Leucosomes contain whitish, cm-sized folded leucocratic bands mainly formed by (saussuritized) plagioclase, quartz, epidote and locally mm-sized titanite crystals (**Figs.2a and Fig.3b**). Such leucosomes have been named trondhjemites by Hervé and Fanning (2003). Melanosomes are characterized by garnet, quartz and epidote and local clinopyroxene (**Figs.2b, c** and **Fig.3c**). The proportion of garnet in the melanosomes can be very variable depending on the degree of melt extraction. Some of the garnet bearing melanosomes that contain more than 50 vol.% garnet are named hereafter garnet-bearing restites (**Fig.3c**). The latter form 10 to 50 cm-thick reddish layers that can be continuously tracked over hundreds of meters (**Fig.2c**). These networks strike mainly N-S, parallel to the HT fabric, in the two localities where they have been

194     identified (**Fig.1c**). At sampling locality #26, several boulders on the seashore exhibit

195     very large, facetted euhedral garnet megablasts (up to 20 cm in diameter) within an

196     amphibolite facies matrix (**Figs. 2d** and **3d**).

197         Importantly, our field observations revealed the presence of felsic gneiss

198     derived from metasedimentary rocks within the Lazaro unit, interleaved with

199     hornblende-bearing mafic lithologies (**Electronic Appendix 1**). These rocks are very

200     retrogressed and now characterized by a large amount of quartz, white mica and, to

201     a lesser extent, hornblende porphyroblasts (e.g., sample #24). Two distinct sampling

202     localities (#22 and #25) also exhibit cm-thick silica-rich layers interbedded with

203     amphibolites and containing numerous garnet crystals that give the rock a reddish

204     appearance (**Fig.3e**). This texture recalls coticules (spessartine quartzites) reported

205     in various localities along the Chilean paleo-accretionary wedge as well as within the

206     underlying blueschist-facies Almagro Complex (Willner et al., 2001; Hyppolito et al.,

207     2016).

208         We finally remark that (i) the Lazaro unit comprises an alternation of

209     decameter-thick metasedimentary layers interbedded within mafic lithologies, (ii)

210     partial melting products are restricted to meter to decameter-thick leucosomes, and

211     (iii) mantle lithologies (e.g. peridotite, serpentinite) are lacking in the studied area.
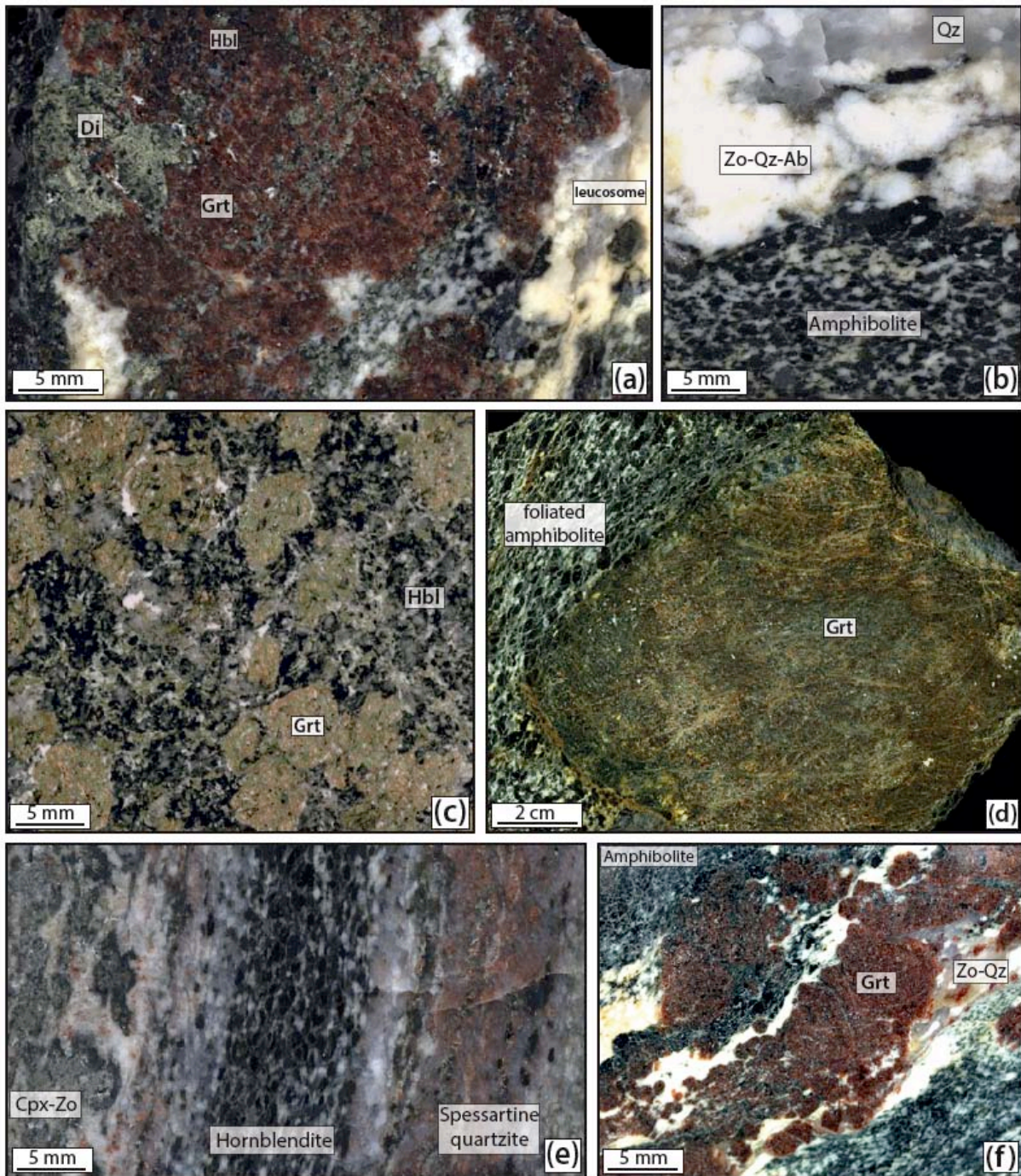
**Figure 3**: Hand specimen photos of Lazaro unit HP-HT rocks. **a**. Polished slab of sample #25 showing a garnet-bearing leucosome comprising peritectic garnet in equilibrium with green diopside and recrystallized melt (mainly formed by quartz and epidote). **b**. Polished slab of a quartz-epidote-feldspar leucosome cutting through the amphibolite matrix (sample #23). **c**. Representative view of a sample from a garnetite layer (garnet-bearing residuum) showing high garnet content (>40 vol.%) and abundant hornblende crystals (sample #25c). Note that garnet has been partly replaced by chlorite during cooling. **d**. Polished section of one of the garnet megablasts shown in picture 2d. This garnet crystal has been wrapped later by an

amphibolite-facies matrix (sample #26b). **e**. Scanned rock slab of a heterogeneous

lithological sequence comprising a diopside-epidote assemblage (left), a hornblendite layer

(middle) and a pinkish spessartine quartzite (right). This sample (#25a) probably corresponds

to a former oceanic volcano-sedimentary rock. **f**. Polished sample showing the preferential

growth of peritectic garnet with quartz-epidote assemblages (former melt) in the middle of an

amphibolite (locality #25).


## 4. ANALYTICAL METHODS


Petrological study has been performed on a set of 20 representative samples

located on **figure 1c**. Electron probe microanalyses were performed at the GFZ

Potsdam with a JEOL-JXA 8230 probe under common analytical conditions (15 kV,

20 nA, wavelength-dispersive spectroscopy mode), using a 10 μm beam. Standards

used for the calibration as follows: orthoclase (Al, Si, K), fluorite (F), rutile (Ti), $Cr_2O_3$

(Cr), wollastonite (Ca), tugtupite (Cl), albite (Na), MgO (Mg), $Fe_2O_3$ (Fe) and

rhodonite (Mn). **Table 1** offers selected analyses of major phases. Elemental XR

maps were obtained with the same machine and with a CAMECA SX-100

microprobe (Center of Scientific Facilities of the University of Granada), using albite

(Na), periclase (Mg), $SiO_2$ (Si), $Al_2O_3$ (Al), sanidine (K), $Fe_2O_3$ (Fe), $MnTiO_3$ (Mn),

$SO_4Ba$ (Ba), $Cr_2O_3$ (Cr), diopside (Ca), $TiO_2$ (Ti) and vanadinite (Cl) as calibration

standards. The images were processed with the software DWImager (Torres-Roldán

and García-Casco, unpublished) (**Fig.6**). To highlight the minerals and textures of

interest, other mineral phases were masked out, and the color images of the phases

of interest were overlain onto a grayscale image base-layer calculated with the

expression $\sum [a.p.f.u./nA/s)_i *A_i$, (where A is the atomic number and i corresponds to

Si, Ti, Al, Fe, Mn, Mg, Ca, Na, Ba, K, P, F and Cl) that contains the basic textural

247 information of the scanned areas. Ternary phase diagrams were calculated using the

248 software CSpace (Torres-Roldán et al., 2000).

249 Amphibole compositions were normalized following the scheme of Leake et al.

250 (1997) with $Fe^{3+}$ estimated using the average normalization-factor. Chlorite and white

251 mica were normalized to 28 and 11 oxygens, respectively, assuming $Fe_{total}=Fe^{2+}$.

252 Garnet and clinopyroxene compositions were normalized to 12 oxygens and 8

253 cations and to 6 O and 23 O, respectively, with $Fe^{3+}$ estimated by stoichiometry.

254 Plagioclase, epidote and titanite were normalized to 8, 12.5 and 5 oxygens,

255 respectively, assuming $Fe_{total}$ as $Fe^{3+}$. Mineral abbreviations used in this work are

256 after Whitney and Evans (2010).

257 Major elements (and some trace elements) were analyzed at GFZ Potsdam by

258 X-ray fluorescence (XRF) prepared as fused discs of Li tetraborate-metaborate

259 (FLUXANA FX-X65, sample-to-flux ratio 1:6), and at ACME Analytical Laboratory

260 (Vancouver, Canada) Ltd., where lithium metaborate fusion and XRF spectrometry

261 were also used. The trace elements were analyzed at GFZ Potsdam and ACME

262 Analytical Laboratory by inductively coupled plasma mass spectroscopy (ICP-MS)

263 after lithium metaborate/tetraborate fusion and nitric acid digestion of 0.2 g of the

264 sample. Loss on ignition was determined gravimetrically after heating the sample

265 powder to 1050°C for 1h. The analyses are given in **Table 2.**

266 In order to provide age constraints for the timing of ductile deformation of the

267 Lazaro unit, we investigated Rb-Sr multi-mineral isotope systematics in samples of

268 white mica-bearing mylonites. Isotopic data was obtained at GFZ Potsdam using a

269 Thermo Scientific TRITON thermal-ionization mass spectrometer. Rb isotope dilution

270 analysis was done in static multicollection mode, and Sr isotopic compositions were

14

271 measured in dynamic multicollection mode. Standard errors for age calculation of ±

272 0.005% for $^{87}$Sr/$^{86}$Sr and ±1.5% for $^{87}$Rb/$^{86}$Sr ratios have been assigned to the

273 results, provided that individual analytical uncertainties were smaller than these

274 values. Mineral separates handling and analytical procedures are described in detail

275 in Glodny et al. (2008). Uncertainties of isotope and age data are quoted at the 2σ

276 level. The program ISOPLOT/EX 3.71 (Ludwig, 2009) was used to calculate

277 regression lines. We used the Rb decay constants recommended by Villa et al.

278 (2015).

279 For the Sm-Nd work, minerals were recovered from small (~50 g) rock

280 fragments using a roll mill for crushing, followed by heavy liquid and magnetic

281 separation techniques. Garnet separates were purified by treatment in 6N HCl in an

282 ultrasonic bath in order to remove adherent apatite. All mineral separates including

283 garnet, apatite, amphibole, titanite and feldspar were finally handpicked under a

284 binocular microscope.

285 Sm-Nd isotopic data were generated at GFZ Potsdam using a Thermo Scientific

286 TRITON thermal ionization mass spectrometer. Nd isotopic compositions were

287 measured in dynamic multicollection mode. Nd and Sm concentrations were

288 determined by isotope dilution using a mixed $^{149}$Sm-$^{150}$Nd tracer, and measured in

289 static multicollection mode. The value obtained for $^{143}$Nd/$^{144}$Nd in the La Jolla Nd

290 standard prior to analysis of samples was 0.511850 ± 0.000004 (n = 7). For age

291 calculation, standard errors of ± 0.002% for $^{143}$Nd/$^{144}$Nd ratios, and ± 0.5% for

292 $^{147}$Sm/$^{144}$Nd ratios were assigned to the results, provided that individual analytical

293 uncertainties were smaller than these values. Otherwise, individual analytical

294 uncertainties were used. Uncertainties of isotope and age data are quoted at 2σ

295    throughout this work. The program ISOPLOT/EX 3.71 (Ludwig 2009) was used to

296    calculate regression lines. Ages quoted here are based on a decay constant $\lambda^{147}Sm$

297    $= 6.54 \times 10^{-12} yr^{-1}$ (Villa et al., 2015).

298        Two kilograms of metasedimentary rock sample #24 were processed to obtain

299    zircons for dating. The U-Th-Pb SHRIMP zircon analyses were performed at the CIC

300    (Centro de Instrumentación Científica) of the University of Granada. Zircon was

301    separated using panning, first in water and then in ethanol. This was followed by

302    magnetic extraction of Fe-rich minerals with a Nd magnet. Finally, zircons were

303    handpicked using a binocular microscope. The zircons were cast on "megamounts"

304    (i.e., 35 mm epoxy discs) fixed on the front of a mount holder so that no metallic parts

305    or surface discontinuities faced the secondary ions extraction plate. The minerals

306    were carefully studied with optical (reflected and transmitted light) and scanning

307    electronic microscopy (backscattering and cathodoluminescence) prior to SHRIMP

308    analyses with the IBERSIMS SHRIMP IIe/mc ion microprobe.

309        Zircons were analysed for U-Th-Pb following the method described by Williams

310    and Claesson (1987). The mount was coated with a c.12 nm thick gold layer. Each

311    spot was rastered with the primary beam for 120 s prior to analysis and then

312    analysed for 6 scans following the isotope peak sequence $^{196}Zr_2O$, $^{204}Pb$, $^{204}Pb$

313    background, $^{206}Pb$, $^{207}Pb$, $^{208}Pb$, $^{238}U$, $^{248}ThO$, $^{254}UO$. All peaks of every scan were

314    measured sequentially 10 times with the following total counting times per scan: 2 s

315    for mass 196; 5 s for masses 238, 248, and 254; 15 s for masses 204, 206, and 208;

316    and 20 s for mass 207. The primary oxygen beam was set to an intensity of about 5

317    nA, with a 120 microns Kohler aperture, which generated 17 x 20 micron elliptical

318    spots on the target. The secondary beam exit slit was fixed at 80 microns, achieving

319    a resolution of about 5000 at 1% peak height. All calibration procedures were

320    performed on the standards included on the same mount. Mass calibration was done

321    on the REG zircon (ca. 2.5 Ga, very high U, Th and common lead content). The

322    analytical session started by measuring the SL13 zircon (Claoue-Long et al., 1995),

323    which was used as a concentration standard (238 µg/g U). The TEMORA zircon

324    (416.8 ± 1.1 Ma; Black et al., 2003), used as an isotope ratios standard, was then

325    measured in between every 4 unknowns. Data reduction was done with the

326    SHRIMPTOOLS software (available from www.ugr.es/~fbea), which is a new

327    implementation of the PRAWN software originally developed for the SHRIMP. Errors

328    are reported at the 95% confidence interval (≈2 σ). Standard errors (95% C.I) on the

329    37 replicates of the TEMORA standard measured during the analytical session were

330    ± 0.35% for $^{206}Pb/^{238}U$ and ± 0.83 % for $^{207}Pb/^{206}Pb$.

331

## 5. PETROLOGY

### 5.1 Microtextures and mineral chemistry

334       5.1.1. *Garnet amphibolite and garnet-bearing restites*

335

336       All the 17 mafic samples from the Lazaro unit studied here were variably

337    affected by retrogression and deformation. In the most re-equilibrated samples, the

338    peak T event is nearly erased and the rocks have been transformed into greenschist

339    facies mylonites (e.g. sample #29a; **Electronic Appendix 2**). Only samples where

340    the HT event is best preserved exhibit rounded diopside crystals included within

341    garnet (**Figs.3a, 3e and Fig.4a**), since matrix diopside is usually pseudomorphed by

342    hornblende (**Fig.4a**). When preserved, clinopyroxene is diopside-rich ($X_{Di}$=0.51-0.64)

343     with Ca-tschermak contents comprised between 0.02 and 0.10 (see **Table 1** for

344     representative analyses).

345          Amphibole comprises brown to deep greenish crystals with compositions

346     varying between pargasite, edenite and hornblende (**Fig.5**). In strongly mylonitized

347     samples hornblende porphyroclasts locally preserve Stage 1 pargasite compositions

348     in the cores as patches, indicating growth of Stage 2 hornblende during cooling after

349     HT conditions (**Fig.5a,b**). The compositional zoning is characterized by nearly

350     constant $Na_B$ (~0.25 a.p.f.u.) and decreasing $Na+K_{(A)}$ (~0.70-0.10) (**Fig.5a**)

351     suggesting cooling at relatively constant pressure. Hornblende is frequently observed

352     at the rims of diopside (**Figs.4a, 5a, b**) or completely replacing former diopside due

353     to the pervasive fracture network affecting garnet crystals. The garnet-diopside peak

354     T assemblage in melanosomes is closely intergrown with leucocratic domains now

355     composed of quartz and a fine-grained mixture of albite and epidote (**Figs.3a, 3f, 4b,**

356     **6a**). This mixture defines rounded to quadrangular shapes and exhibits integrated

357     composition roughly corresponding to a Na-Ca plagioclase. Plagioclase is almost

358     systematically replaced by this mixture except one small inclusion in a garnet core

359     with oligoclase composition ($An_{24}$; **Table 1**). **Figure 6c** shows one former plagioclase

360     inclusion replaced by a Na-rich feldspar included within a garnet crystal that shows

361     enrichment in Grs component ($Grs_{91}Alm_7Sps_2$) around the inclusion, likely by means

362     of the decomposition of the pristine plagioclase (plagioclase = albite + epidote +

363     grossular-rich garnet).

364

18
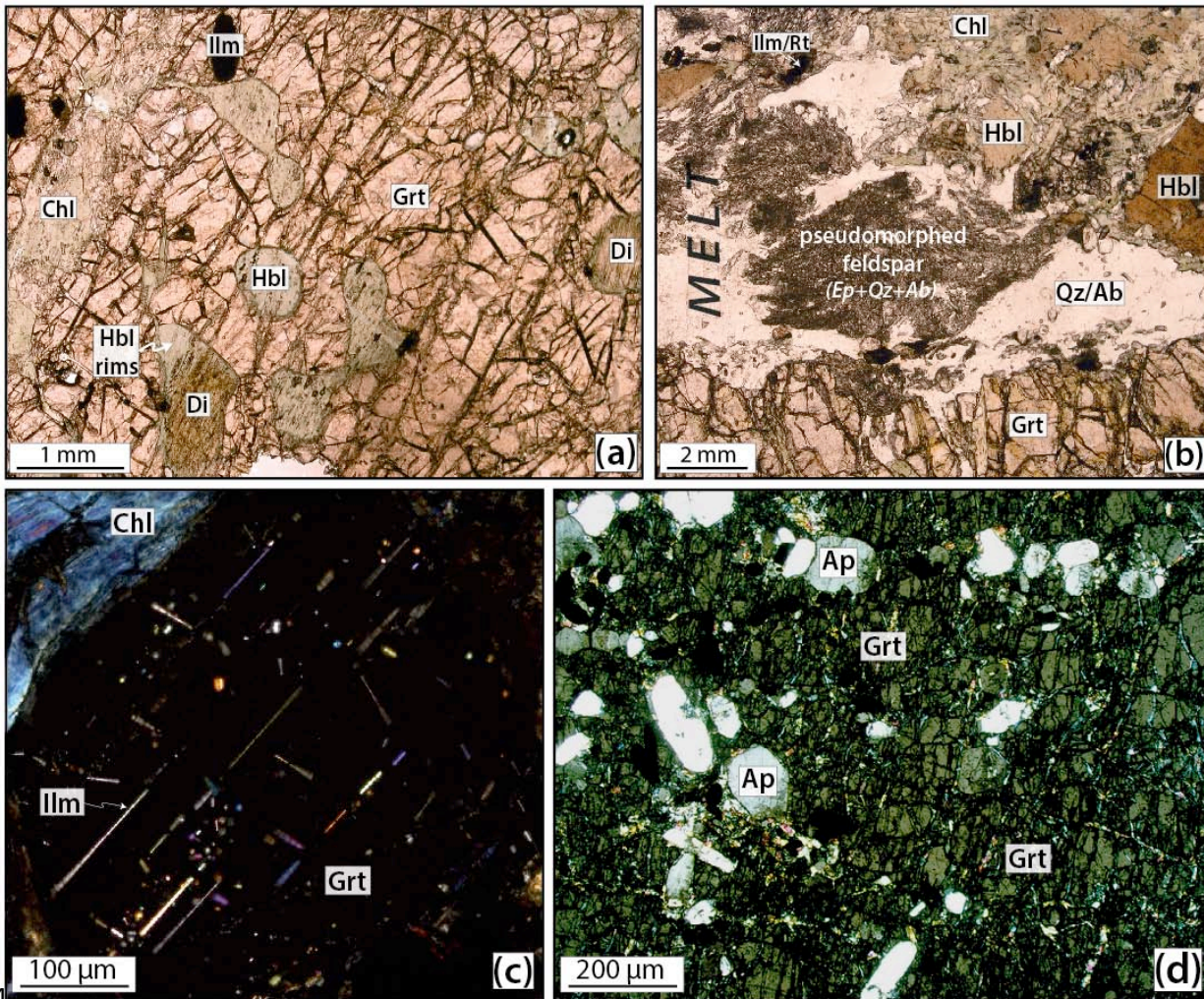
**Figure 4**: Optical microscope pictures. **a**. Rounded diopside inclusions within garnet, partly replaced by hornblende (sample #2-31). Note the strong fracturing of garnet and the partial replacement by chlorite. **b**. Image showing microtextural relationships between garnet, the leucosome and hornblende (sample #25). Plagioclase crystals are now replaced ('saussuritized') by a fine-grained mixture of albite and zoisite-rich epidote. **c**. Cross-polarized view of a garnet crystal (sample #26b) showing exsolved ilmenite and rutile needles defining a geometric network. Note that this garnet is compositionally homogeneous (no zoning). **d**. View showing the abundance of apatite inclusions in the garnet megablast used for Sm-Nd dating (sample #26b; crossed-polarized view).

Two generations of epidote have been texturally identified. The first generation ($Ps_{10-15}$) is tightly intergrown with quartz forming a myrmekite-like texture (cf. Shelley, 1967) around peritectic garnet (see below) within garnet bearing restites (**Fig.6b**).

378     The second generation (Ps$_{15-25}$) is ubiquitous in Lazaro rocks and forms after

379     replacement of Na-Ca plagioclase. It typically exhibits two pseudomorphic habits: (i)

380     fine grained intergrowths of albite and epidote (**Fig.6a**), (ii) coarse grained radiating

381     epidote crystals.

382
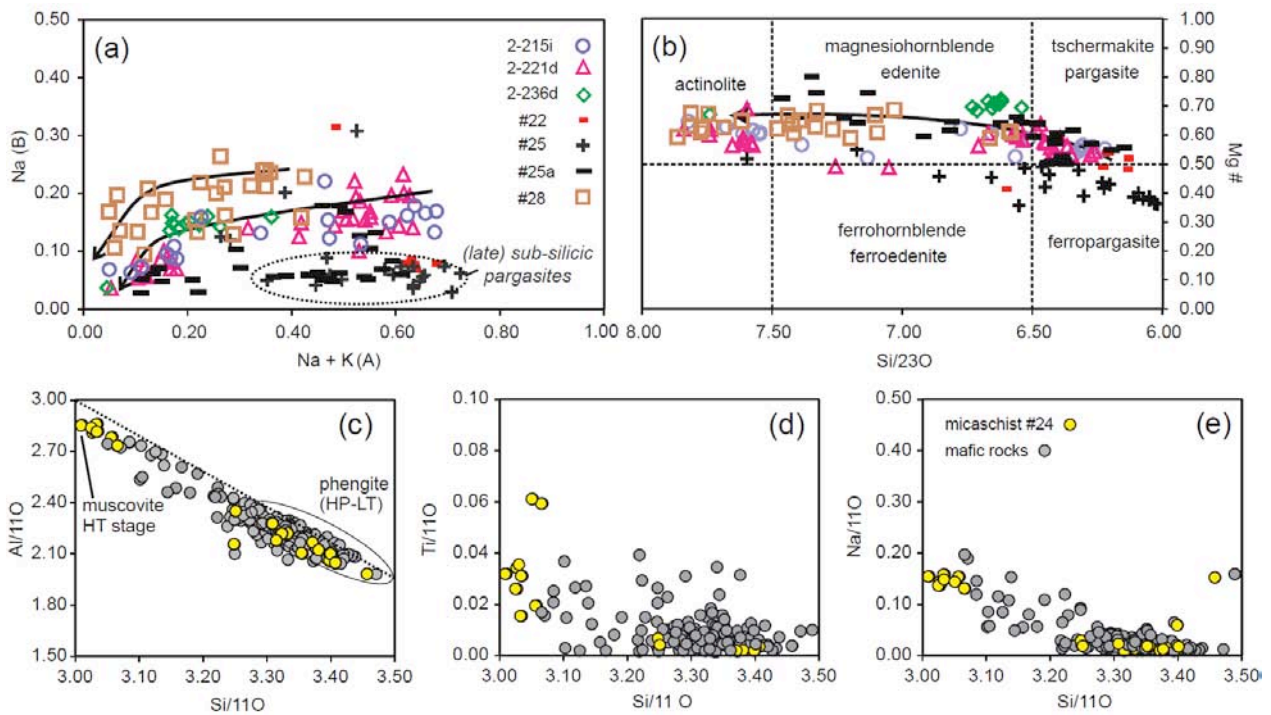


384   **Figure 5**: Electron probe data on amphibole and white mica. **a** and **b**. Chemical composition
385   of amphibole according to the classification of Leake et al. (1997). The arrow symbolizes the
386   core-to-rim composition zoning observed in analyzed amphibole. **c, d** and **e**. Plot of white
387   mica composition showing the variation of Al, Ti and Na contents as a function of silica
388   content. The dashed line in c indicates the ideal Tschermak substitution.

389

390     We also report the presence of rounded polymineralic inclusions (20-40µm in

391     diameter) within garnet grains (**Fig.6d**). The inclusion shown in **Figure 6d** contains

392     albite, titanite, muscovite and chlorite. The size, presence of low-angle boundaries

393     and composition of these inclusions contrast with those of the aforementioned

394     pseudomorphs after plagioclase in garnet. Retrogression-related microfracturing is

395     responsible for retrogression and the growth of LT minerals within the inclusion.

396         A network of exsolved 2 µm ilmenite and rutile needles are locally present

397     within garnet (**Fig.4c**), in particular within megablasts (**Fig.3d**). These megablasts

398     also contain numerous, 50-500 µm apatite crystals as well as numerous ilmenite

399     crystals (**Fig.4d**). Ilmenite is frequently observed in Lazaro unit garnet amphibolites,

400     locally rimmed by rutile (**Fig.6e**). Rutile forms euhedral grains and needles included

401     within pargasite. In sample #25, 100-250 µm titanite porphyroblasts are included

402     within garnet, pargasite cores and leucocratic domains.

403         Garnet occasionally exhibits some zoning. Garnet I generation (cores) is

404     weakly zoned. It is often rimmed by a variably thick garnet II generation with lower

405     Mg content (typically 0.05-0.15; **Fig.7**). Complex networks of healed fractures with

406     much lower XMg compositions and higher Mn and Ca contents are present in garnet

407     II (**Figs.7a, 7b and 7c**).

408         Zoned white mica crystals exhibit muscovite cores rich in Ti and Na, in

409     contrast to phengite-rich rims (Si=3.35-3.4 a.p.f.u.) that developed around them

410     (**Fig.5c, 5d and 5e**). Biotite is rare and only observed included in garnet or pargasite

411     cores (**Table 1**).
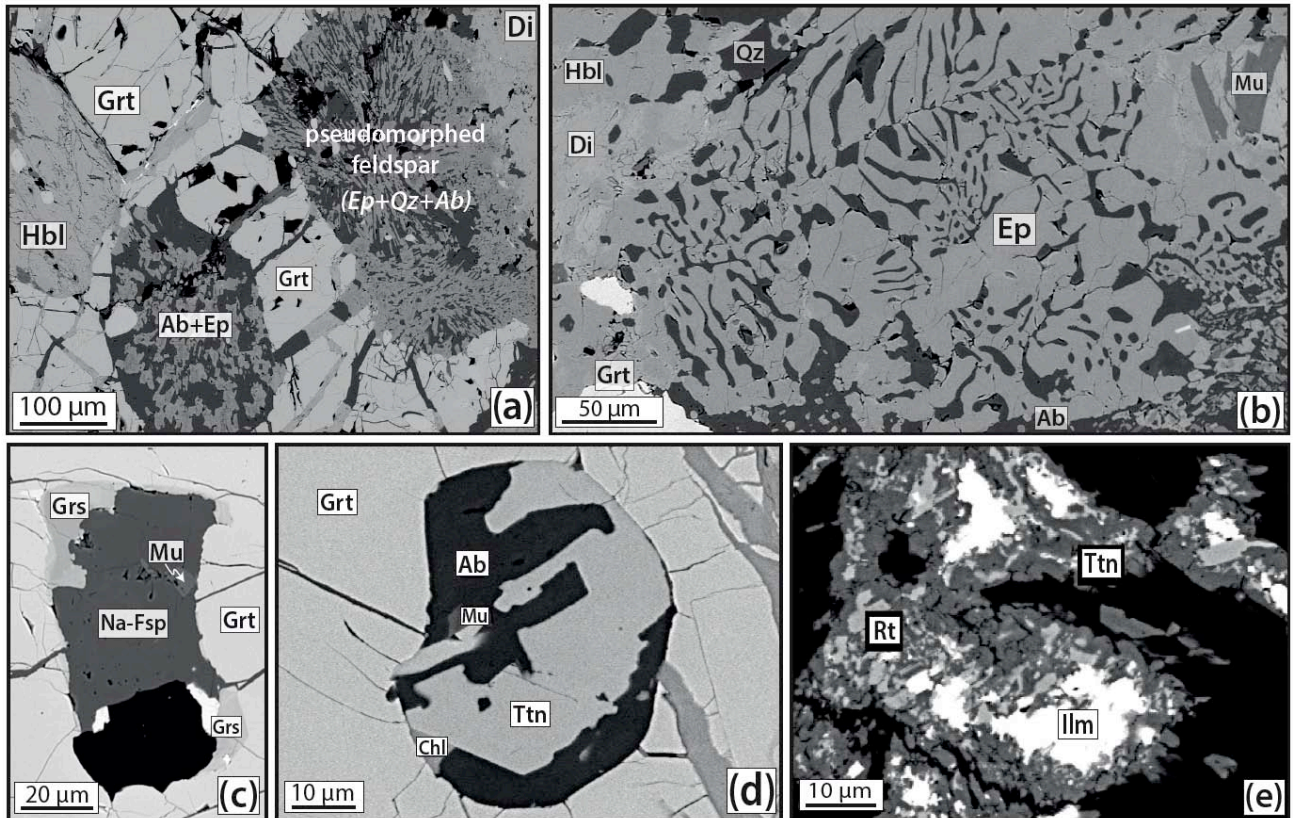
**Figure 6**: Back scattered electrons images obtained at the scanning electronic microscope. **a**. Inclusions of former Ca-Na plagioclase in garnet now fully replaced by a mixture of albite, epidote ± quartz (sample #25). **b**. View of a myrmekitic ("vermicular") zoisite-rich epidote crystal showing intergrowth features with quartz (dark grey; sample #25a). **c**. Inclusion of Na-feldspar in a garnet crystal (sample #25a). A discontinuous rim of grossular garnet forms at the contact between the inclusion and the host. **d**. Rounded, poly-mineralic inclusion included in garnet from sample #25c. **e**. HT ilmenite is rimmed by rutile, which is overgrown and replaced by titanite during cooling.
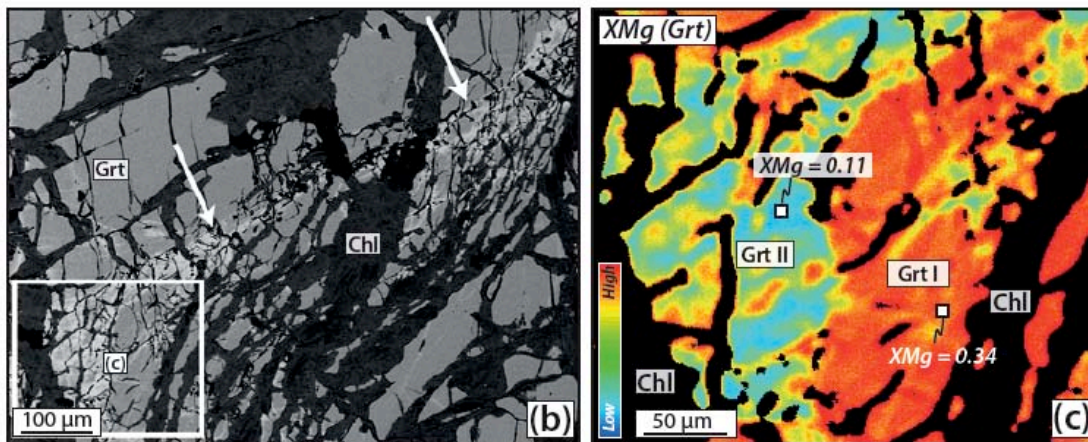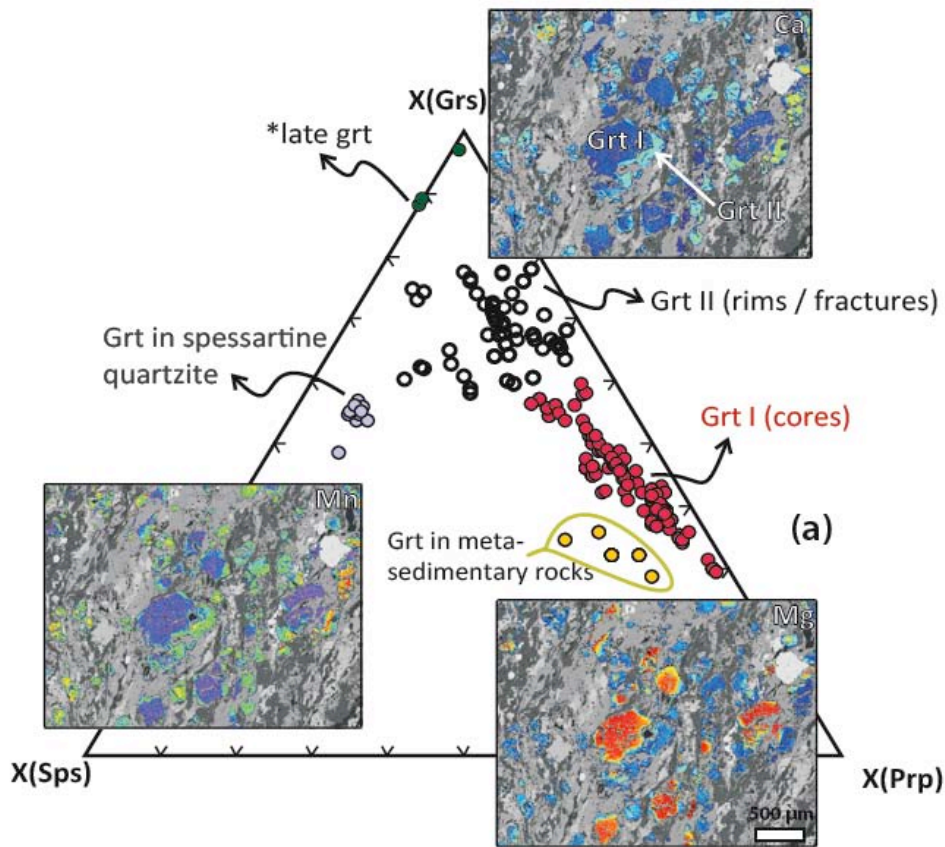
**Figure 7**: Garnet chemical zoning and composition. **a**. Triangular plot showing the composition of Lazaro unit garnet crystals. Garnet from spessartine quartzite plot closer to the Sps corner while Ca-rich garnet observed around the inclusion shown in Fig.5c corresponds to a grossular composition (green circles). Three X-ray maps (Ca, Mn, Mg) provide a representative view of dismembered HT garnet crystals rimmed by higher Ca-Mn and poorer Mg rims. **b**. BSE image of a fossilized fracture network (white arrows) cutting through a HT garnet from sample #21. **c**. X-ray map of the same crystal showing a decrease of the XMg content along the healed fracture network.

431

Mineral assemblages developed during cooling comprise combinations of

phengite, chlorite, epidote ($Ps_{20\text{-}30}$), hornblende, actinolite and titanite (**Fig.8**).

Phengite (Si=3.4-3.45 a.p.f.u.) is visible along garnet cracks in the least deformed

samples and parallel to the foliation in the most sheared samples (**Table 1**). Chlorite

frequently replaces garnet along cracks and also defines the foliation intergrown with

phengite flakes. In sample #25c, two chlorite generations (XMg=0.6 and 0.4) suggest

multiple re-equilibration stages during cooling. Actinolite is systematically observed

around hornblende crystals (**Figs.5a, b**). Titanite replaces ilmenite-rutile aggregates

(**Fig.6e**). The paragenetic evolution of mafic samples as a function of the main

metamorphic stages identified here is summarized in **Figure 8**. Importantly,

orthopyroxene has not been found despite extensive investigation and a systematic

check of garnet inclusions.

A texturally late generation of pargasite has been observed in three samples

(**Electronic Appendix 1**, **Fig.5a and 5b**). It comprises post-kinematic crystals with

sub-silicic composition, low $Na_B$ (< 0.10 apfu) and  $Na+K_A$ contents varying from

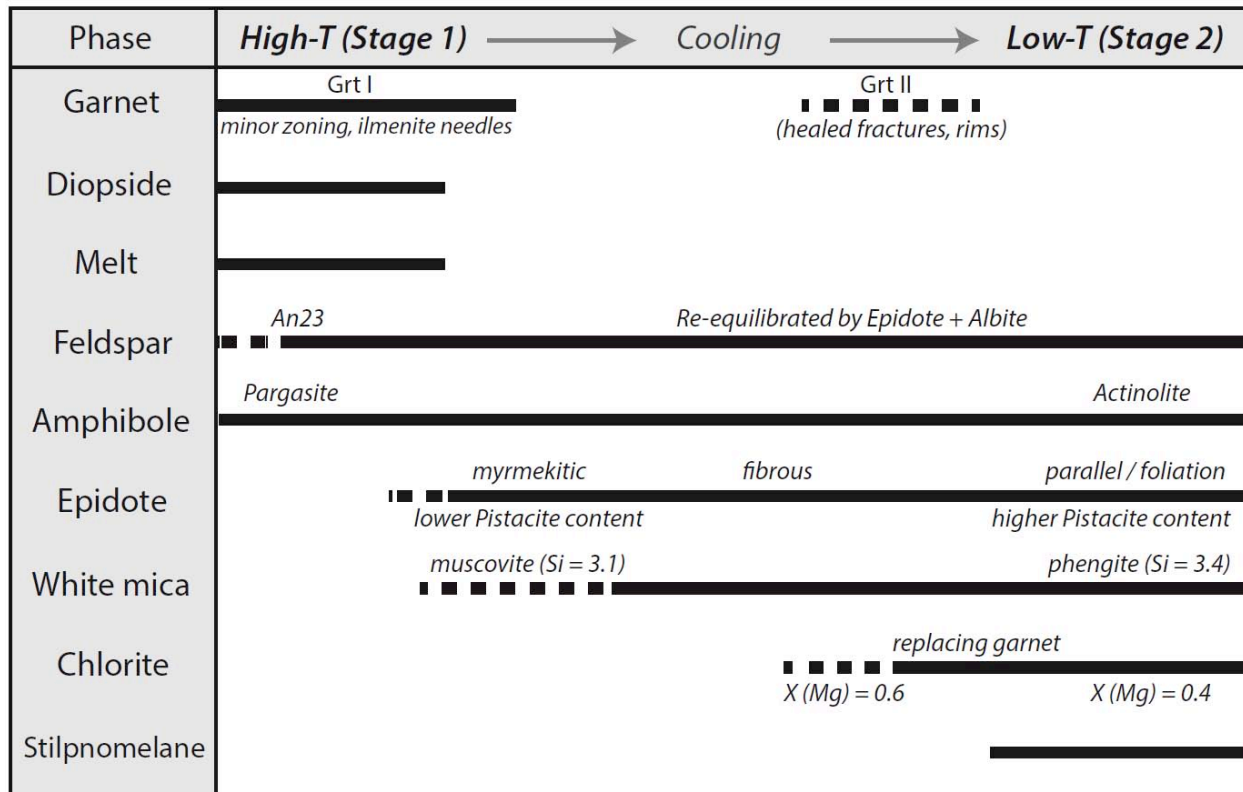~0.70 to 0.35, likely recording discrete and later shallow heating (see below).

### 5.1.2 *Trondhjemitic leucosome*

Sample #25b (**Fig.3b**) corresponds to a fine-grained mixture of 10-20 μm

crystals of epidote, albite, muscovite and quartz with locally large porphyblasts of

titanite. The presence of diffuse quadrangular shapes in the leucosome suggests the

former presence of mm-sized plagioclase crystals now dominantly replaced by

epidote and albite. Muscovite crystals are small (<50 μm; 3.05-3.1 Si a.p.f.u.), rare

24

455 (<2 vol.%) and rimmed by phengite (typically 3.35-3.4 Si a.p.f.u.). Epidote ($Ps_{15-20}$)

456 often preserves Fe-poorer cores ($Ps_{5-10}$).

457



| Phase | *High-T (Stage 1)* $\longrightarrow$ *Cooling* $\longrightarrow$ *Low-T (Stage 2)* |
|---|---|
| Garnet | Grt I — *minor zoning, ilmenite needles* — Grt II (*healed fractures, rims*) |
| Diopside | |
| Melt | |
| Feldspar | *An23* — *Re-equilibrated by Epidote + Albite* |
| Amphibole | *Pargasite* — *Actinolite* |
| Epidote | *myrmekitic* — *fibrous* — *parallel / foliation*; *lower Pistacite content* — *higher Pistacite content* |
| White mica | *muscovite (Si = 3.1)* — *phengite (Si = 3.4)* |
| Chlorite | *replacing garnet*; *X (Mg) = 0.6* — *X (Mg) = 0.4* |
| Stilpnomelane | |

458

459 **Figure 8**: Occurrence table summarizing the petrological evolution of Lazaro unit samples
460 throughout their metamorphic evolution.

461

462        5.1.3 *Metasedimentary rocks*

463      Three metasedimentary samples interleaved with mafic lithologies have been

464 studied in detail: a mica schist (#24) and two spessartine quartzites (#22 and #25a;

465 **Fig.3e**). The mica schist exhibits abundant muscovite crystals (3.01-3.07 Si a.p.f.u.)

466 rimmed by phengite-rich compositions (3.3-3.47 Si a.p.f.u.; **Figs.5c, 5d and Fig.9a**).

467 These Si-rich rims are in textural equilibrium with chlorite that replaces garnet

468 crystals. In the spessartine quartzite (sample #25a), a former K-feldspar micro-

469  domain is replaced by aggregates of white mica with Ba-rich muscovite cores (up to

470  BaO= 3 wt.%, Si= 3.1 a.p.f.u.) and Ba-depleted phengite rims in textural equilibrium

471  with interstitial albite (**Fig.9b**). Garnet crystals from such layers typically range

472  between 10 and 35 mol.% spessartine component. In the X-ray maps from **Figure**

473  **7a**, it is clearly visible that HT Mg-rich garnet I cores are rimmed by 100-200 µm thick

474  Ca-Mn-Fe richer garnet II rims which, in turn, are partly replaced by chlorite. Note

475  that chlorite Mg content spatially varies in **Figure 9a** suggesting progressive and

476  partial re-equilibration during cooling. Epidote cores ($Ps_{7-12}$) exhibit minor zoning with

477  slight increase in ferric iron towards the rims ($Ps_{20-22}$). When present, amphibole

478  shows a compositional zoning similar to the one described for garnet amphibolites

479  with edenitic-pargasitic cores grading to hornblende rims (**Fig.5**). Other accessory

480  minerals are titanite (overgrowing ilmenite/rutile), apatite, pyrite and zircon. Graphite

481  has not been observed.

482

483    **5.2    Phase relations**

484

485    The projections presented below have been calculated with software *Cspace*

486  (Torres-Roldán et al., 2000) and a similar approach to that used by Garcia-Casco et

487  al. (2008) has been applied to the graphical representation of melting phase relations

488  in mafic systems at peak metamorphic conditions. The diagrams are projected from

489  coexisting phases and exchange vectors that allow for complete representation of the

490  compositional space and peak metamorphic mineral compositions. For simplicity, all

491  projections have been made through $H_2O$, implying $P_{H2O} = P_{total}$, and Fe is treated as

492  $FeO_{total}$. Note that projection along the plagioclase exchange vector $SiNa(AlCa)_{-1}$

26

493 makes albite and anorthite colinear in the ACF diagram, hence preventing

494 discrimination between HT Na-Ca plagioclase and LT albite.

495



496
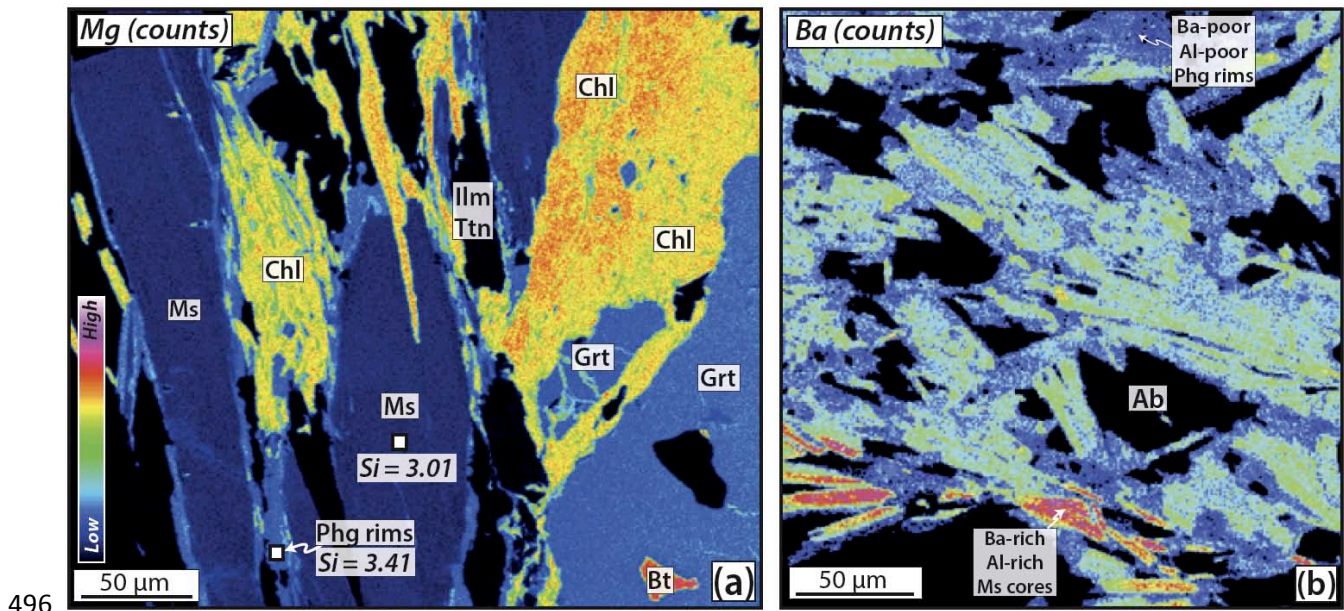
**Figure 9**: X-ray maps of metasedimentary rocks from the Lazaro unit. **a**. Mg content map showing the effect of Tschermak substitution visible as high Mg, Fe and Si contents in the rims that form around muscovite rims (sample #24). Note the heterogeneous zoning pattern of chlorite, partly replacing garnet. **b**. X-ray map showing the barium content of a pseudomorph after K-feldspar in sample #25a. Barium-rich zones match with Al-richer muscovite cores while Ba-depleted crystals exhibit lower aluminum contents.

503

504         5.2.1 *ACF diagram*

505      The near-peak metamorphic event for garnet amphibolite is represented by

506 the assemblage pargasite+epidote±garnet±diopside±Na-Ca plagioclase. Peak

507 topologies are mainly defined by whole rock compositions plotting along the tie-line

508 epidote-amphibole and inside the tie-triangles epidote-pargasite-garnet and epidote-

509 clinopyroxene-garnet (**Fig.10a**). The high extent of greenschist facies overprint

510 prevents concluding whether epidote and/or plagioclase were stable at peak

27

511     conditions or if the phase relations shown in the ACF diagram represent near-peak

512     conditions slightly after reaching peak temperature. The presence of myrmekite-like

513     intergrowths of epidote and quartz around garnet confirms that epidote has likely

514     been involved in both garnet forming and garnet consuming reactions. As in other

515     instances of (hydrous) melting of mafic rocks, plagioclase may have been totally

516     consumed during melt formation (e.g., García-Casco et al., 2008, and references

517     therein). Samples plot within the tie-triangle plagioclase-amphibole-garnet suggesting

518     that for these bulk compositions plagioclase should have been present during peak

519     conditions. This implies retention of partial melt and crystallization of plagioclase (and

520     epidote minerals) during melt crystallization.

521     The trondhjemite sample #25b (former melt) plots close to the line separating

522     metaluminous and peraluminous fields of the ACF projection (**Fig.10b**), showing that

523     plagioclase, epidote and pargasite can crystallize from this melt composition.

524     Muscovite may also crystallize from this melt, as shown in the ACF diagram of

525     **Figure 10b** by the tie-triangle Pl-Ms-Ep (note that crossing of tie-lines in **Figure 10b**

526     represents an artefact of the condensation of the composition space due to projection

527     along the $KNa_{-1}$ exchange vector rather than potential reactions between these

528     phases). The local observation of muscovite inclusions within garnet corroborates

529     this statement.

530
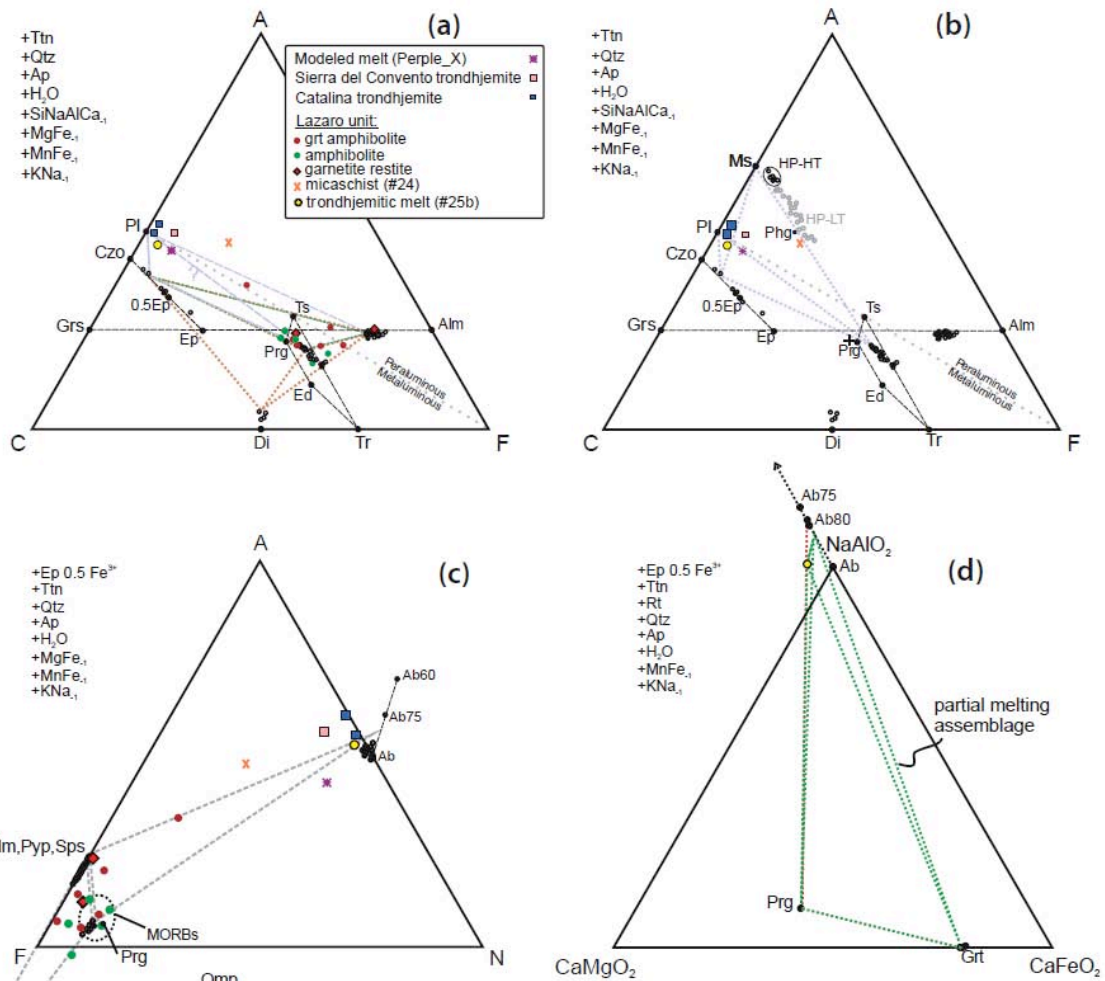
**Figure 10**: ACF, AFN diagrams (a-c) and AFM-like diagram (d) showing peak near-metamorphic and melt-related assemblages of representative samples of mafic rocks from Lazaro unit. Some mineral end-members and analyzed mineral compositions are plotted. Also bulk trondhjemite compositions from Sierra del Convento (Cuba; Garcia-Casco et al., 2008) and from the Catalina Island (samples 3755 and 3754 from Sorensen, 1988) are plotted for comparison. **a**. ACF diagram of garnet amphibolite and amphibolite. Dashed green lines: tielines connecting epidote, garnet and pargasite. Dashed brown lines: tielines connecting epidote, diopside, pargasite and garnet. Dashed purple lines: tielines connecting plagioclase, epidote, pargasite and garnet (see text for explanation). **b**. ACF diagram representing magmatic minerals that can crystallize from the melt. **c**. AFN diagram of garnet amphibolite and amphibolite. Dashed gray lines connecting diopside, garnet and pargasite

(left lower triangle), and garnet, pargasite and plagioclase (An$_{80}$) (right upper triangle). The area defined by the black dashed line comprises the MORBs position in the projection. See text for explanation. **d**. AFM-like diagram representing partial melting assemblages. The red dashed line represents the degenerated phase relationships defined by the alignment of pargasite, melt and plagioclase (An$_{77}$). The green dashed line connects pargasite, melt, garnet and plagioclase (Ab$_{85}$) representing a peritectic reaction with melt and garnet as products. See text for explanation.

### 5.2.2 AFN diagram

For peak conditions the larger part of Lazaro samples plots along the tie-line Prg-Grt and within the tie-triangle Grt-Prg-Di in the AFN diagram projected from (clino)zoisite/epidote (**Fig.10c**). This projection also shows that for compositions slightly richer in Na$_2$O and/or Al$_2$O$_3$, plagioclase can coexist in equilibrium with pargasite and garnet (upper right triangle in **figure 10c**). This suggests that samples plotting in the tie-triangle Grt-Prg-Di have experienced a certain <span style="color:red">amount</span> of melt extraction with respect to potential MORB protoliths, if plagioclase was totally consumed to generate melt. The presence of numerous Na-Ca plagioclase crystals (now pseudomorphed) suggests that plagioclase was in equilibrium with high-T phases shortly before peak conditions. This projection also reveals that for a melt composition plotting within the tie-triangle Grt-Prg-Pl the composition of the plagioclase should be around Ab$_{80}$, similar to the relict inclusions of plagioclase within garnet.

### 5.2.3 NaAlO$_2$−CaMgO$_2$−CaFeO$_2$ diagram

In order to track the composition of the plagioclase involved in melt-producing reactions in mafic rocks, an "AFM-like" projection has been used simulating a

571 possible garnet-absent reaction (**Fig.10d**). The latter type of reaction provides a

572 unique analytical solution for the composition of plagioclase, provided that melt

573 composition is fixed (trondhjemite #25b) and considering the colinearity of the phases

574 involved (plagioclase, melt and amphibole) (see García-Casco et al., 2008 for

575 details). For a plagioclase composition of $Ab_{77}$, a degenerate phase relation is

576 defined of the form:

577 $$Pl + Qtz + Ep + Amp (+ H_2O) = melt + Ttn.$$

578 This reaction is characterized by colinearity of plagioclase-pargasite and melt

579 in **Figure 10d**, implying a large amount of plagioclase was used to form the melt

580 composition and no formation/consumption of garnet and diopside (i.e., it applies

581 only to garnet/diopside-lacking rocks such as leucosomes; cf. Garcia-Casco et al.,

582 2008). It is worth noting that this degenerate phase relation was likely the exception

583 rather than the rule. There is no reason to claim a prevalence of colinear relations in

584 such a high-variance metamafic chemical system. For Na-richer plagioclase

585 compositions, the phase relationships change from a colinear plagioclase-melt-

586 pargasite topology to the peritectic relation depicted by the reaction:

587 $$Amp + Pl + Ep + Qtz (+ H_2O) = melt + Grt,$$
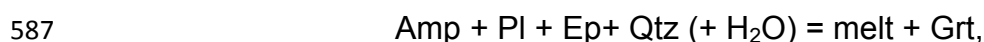
588 while the garnet consuming reaction:

589 $$Amp + Pl + Grt + Qtz (+ H_2O) = melt + Ep$$
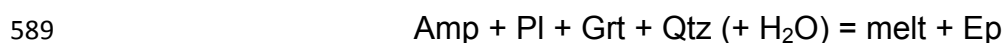
590 occurs for Ca-richer plagioclase (cf García-Casco et al., 2008). In the case of the

591 Lazaro unit, the peritectic garnet-forming reaction took place, as indicated by the

592 formation of porphyroblastic and megablastic garnet in melanosomes.

31

593    The approach presented above graphically confirms the involvement of sodic

594    plagioclase ($Ab_{77}$) in the peritectic garnet-forming reactions. This inference can be

595    extended to the case of diopside-bearing assemblages and for the general case of

596    either $H_2O$-saturared or $H_2O$-subsaturated systems (e.g., Green, 1982; García-Casco

597    et al., 2008).


598

599    **5.3 Bulk rock geochemistry**

600

601    *5.3.1    Mafic rocks*

602

603    Garnet amphibolite and amphibolite show basic compositions with $SiO_2$

604    varying between 41 to 52 wt.%, corresponding to tholeiitic basalt and picro-basalt

605    ($Na_2O + K_2O$ = 0.34 to 4.26, **Table 2**). One mafic orthogneiss is richer in $SiO_2$ (55.54

606    wt.%) and plots in the basaltic andesite field due to the presence of a thin metachert

607    band (which does not impact the trace element pattern typical of a MORB). To

608    constrain the tectonic setting in which the protoliths of garnet amphibolite and

609    amphibolite formed, the pattern of trace elements with relatively immobile behavior

610    during (low temperature) seafloor alteration and high temperature metamorphic

611    conditions have been considered (mainly HREE and some HFSE).

612    Garnet amphibolite and amphibolite have a nearly flat chondrite-normalized

613    REE pattern and are distributed between average N-MORB and E-MORB

614    compositions (**Fig.11a,b**). Their composition overlaps with blueschists and garnet

615    amphibolites from the underlying HP-LT Almagro Complex (**Fig.11a**). Samples with

616    anomalous patterns have been plotted separately (**Fig.11b**). These patterns suggest

617    modifications due to (i) melt extraction/garnet fractionation in garnet-bearing rocks

32

618   (relatively higher HREE concentrations with respect to enriched MORBs and

619   negative Eu anomaly); (ii) late hydrothermal/metasomatic processes (positive Eu

620   anomalies and fractionated pattern characterized by lower HREE contents in

621   "pegmatite-like" samples); (iii) retrogression-related contamination characterized by

622   slightly higher LREE concentrations in garnet amphibolites with evidence of melt loss

623   (e.g., samples of case (i)).

624   The Y-La-Nb diagram (Cabanis and Lecolle, 1989) is useful for discriminating

625   basalts formed in convergent and extensional settings. **Figure 11c** reveals the non-

626   orogenic affinity of the Lazaro unit rocks, which mainly plot in the field of extension-

627   related oceanic basalts, and are distributed along the N-MORB-E-MORB-OIB trend.

628   Three samples plot within the field of possibly contaminated undifferentiated basaltic

629   magmas or continental basalts, likely reflecting local La enrichments. The Th/Yb

630   versus Nb/Yb diagram of Pearce (2008) (**Fig.11d**) is suited to track mantle sources

631   (Nb/Yb) and the effects of crustal components (Th/Yb), making use of two highly and

632   nearly equally incompatible elements in basaltic magmas (Th and Nb).  However,

633   these two elements have different behaviors during subduction, being non-

634   conservative and conservative, respectively, hence defining a sensitive indicator of

635   crustal involvement due to magma–crust interaction or to inheritance of subduction

636   components (Pearce, 2008). In the Th/Yb vs Nb/Yb diagram (**Fig.11d**) Lazaro rocks

637   are distributed between N-MORB and E-MORB, confirming their oceanic affinity (with

638   minor crustal contamination for some samples).

639
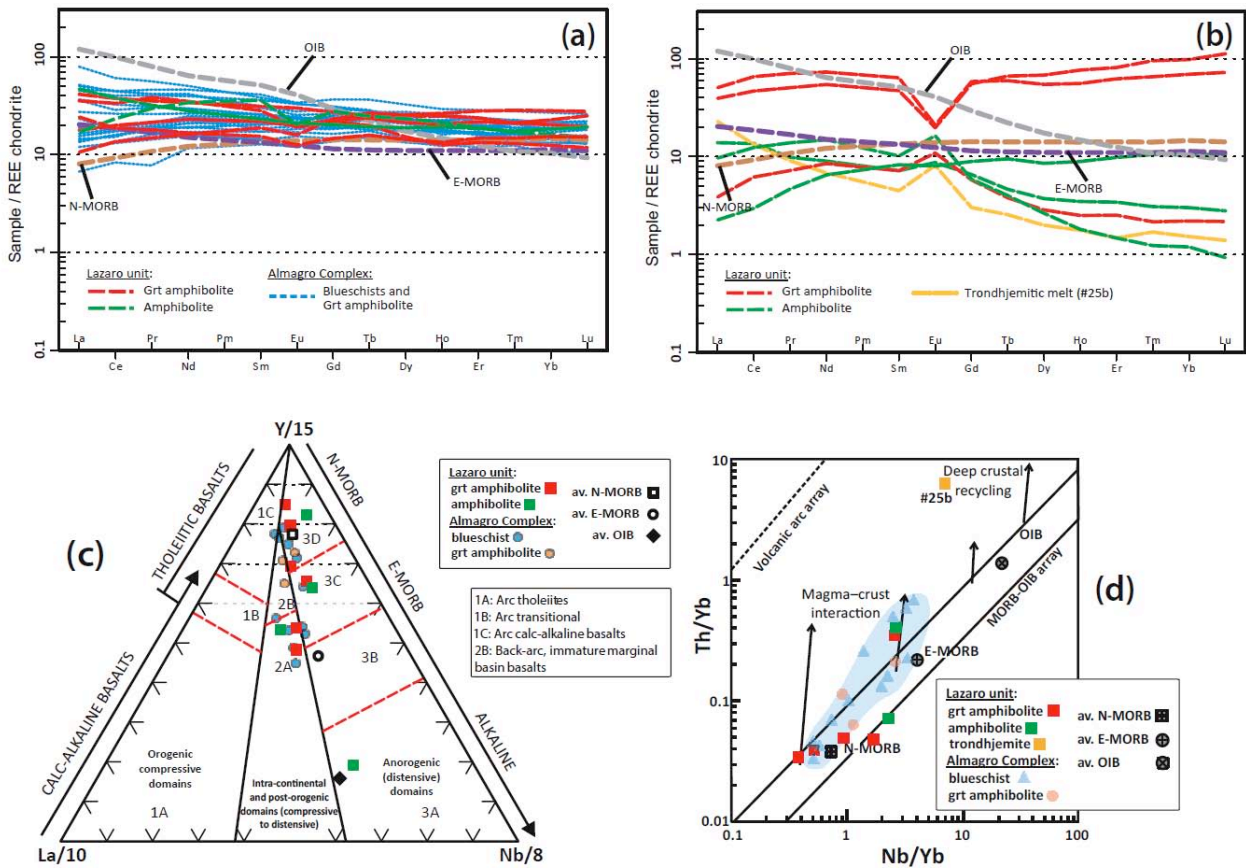
**Figure 11**: Geochemical data on Lazaro unit rocks. **a**. REE plot of garnet amphibolite and amphibolite from the Lazaro unit. This data is compared with underlying metabasalt from the Almagro Complex (Hyppolito et al., 2016). OIB, N-MORB and E-MORB compositions from Sun and McDonough (1989). **b**. REE plot for more samples from the Lazaro unit departing from the global trend. Those anomalous compositions may be related to melt extraction and/or garnet crystallization processes. **c-d**. Y-La-Nb diagram of Cabanis and Lecolle (1989) and Th/Yb versus Nb/Yb diagram of Pearce (2008), respectively, showing the oceanic affinity of Lazaro rocks.

### 5.3.2 Trondhjemitic leucosome

Sample #25b belongs to the trachyte field in the TAS classification (total alkalis-silica), with 61 wt.% $SiO_2$, high $Na_2O$ (8.02 wt.%) and very low $K_2O$ (0.68 wt.%) contents, low contents of $FeO_t$ and MgO (1.27 wt.%, 0.59 wt.%, respectively), and high mg# (0.45, **Table 2**). This sample is classified as trondhjemite, following the

656     molecular normative (CIPW) Ab-An-Or diagram of O'Connor (1965) and the fields of

657     Barker (1979) (not shown), and it is slightly peraluminous with an Alumina Saturation

658     Index (ASI) of 1.17, plotting at the transition between metaluminous (0≤ASI≤1) and

659     peraluminous fields (1≤ASI≤ 3) (not shown). The chondrite-normalized REE pattern

660     shows enrichment in light REE (LREE) revealing a fractionated pattern (**Fig.11b**).

661     The positive Eu anomaly corroborates the presence of plagioclase in melt forming

662     reactions. It is also in agreement with negative Eu anomalies in garnet bearing

663     samples with evidences of melt loss.


664

665     **6.     THERMOBAROMETRY**

666         **6.1     Single-equilibrium thermobarometry**

667

668         In order to constrain the temperature reached by the Lazaro unit rocks during

669     the HT metamorphic event, the garnet-clinopyroxene thermometers of Ravna (2000)

670     and Ellis and Green (1979) have been used for samples #25 and #2-31b, in which

671     peak metamorphic diopside has been preserved during retrogression. These

672     temperatures have been calculated for a fixed pressure of 1.2 GPa. This pressure

673     estimate was obtained on a garnet amphibolite sample (#27) following the calibration

674     of Kohn and Spear (1990) for Grt-Amp-Pl-Qz assemblages. Averaged results are

675     given in **Table 3**. Temperature estimates based on Ravna (2000) yield c. 50°C cooler

676     temperatures than those based on Ellis and Green (1979). These results suggest

677     that the Lazaro unit reached peak temperatures in the range 700-780°C.


678

679         **6.2     Chlorite-phengite thermobarometry**

680

681    In order to estimate the P-T conditions for the retrogression of Lazaro unit

682    rocks, we used for sample #29a an approach similar to the one initially developed by

683    Berman (1991) (see detailed results and approach in **Electronic Appendix 2**). The

684    MATLAB software "Kit Chl-Phg" has been used here to perform these calculations

685    (method and thermodynamic database used is described in Vidal et al., 2001,

686    Dubacq et al., 2010 and Angiboust et al., 2014). This software enables a statistical

687    exploration of chlorite-phengite pairs and the identification of equilibria between end-

688    members. The multivariant reactions are manually plotted and P-T conditions for

689    curve intersection are derived. For sample #29a, 28 equilibria satisfying validity

690    criteria have been found. The average of these estimates yields a temperature of 541

691    ± 59°C and a pressure of 1.12 ± 0.19 GPa. Despite a relatively large spread, these

692    results indicate that the retrograde path (Stage 2) proceeded under relatively high

693    pressures, similar to stage 1 pressure conditions.

694

695    **6.3    Pseudosection modeling**

696

697    The P-T location of the peak metamorphic assemblage and the nature of melt-

698    producing reactions have been investigated using the pseudosection modeling

699    approach and the software package Perplex (v.6.7.2; Connolly, 2005). Evaluating the

700    effective bulk rock composition is difficult because these rocks have been subject to

701    variable degrees of melt extraction/infiltration. Therefore, none of the bulk rock

702    compositions given here can be used to model phase relationships at pre-peak

703    conditions. Trace-element composition and phase relationships (**Fig.11**) have shown

704    that most Lazaro rocks originally derive from a protolith close to a MORB

705    composition. Hence, we decided to use an average of c. 5000 glass analyses

36

706　compiled from the PetDB database (http://www.earthchem.org/petdb; composition

707　given in **Fig.11**). The thermodynamic modeling has been performed in the

708　NCKFMASH system (manganese and ferric iron have been neglected for simplicity).

709　Activity models used here are the following: garnet and biotite (White et al., 2007),

710　clinopyroxene (Holland and Powell, 1996), orthopyroxene (Powell and Holland,

711　1999), amphibole (Dale et al., 2005), chlorite (Holland et al., 1998), white mica (Smye

712　et al., 2010), melt (White et al., 2001 and White et al., 2007), and feldspar (Fuhrman

713　and Lindsley, 1988).

714　The amount of $H_2O$ in the system is a critical parameter as it influences the position

715　of the solidus as well as the amount of melt produced (e.g. Vielzeuf and Schmidt,

716　2001). We first ran a T-[$H_2O$] pseudosection for a fixed pressure of 1.2 GPa in order

717　to assess the optimal amount of water needed to accurately reproduce petrogenetic

718　observations (**Fig.12a**). This diagram shows that the observed peak paragenesis of

719　hornblende-garnet-diopside-feldspar±quartz is achieved for a T range between 670

720　and 780°C and initial water amounts between 1.5 and 3.5 wt.%. **Figure 12b** shows

721　modal amounts of peak metamorphism mineral phases as a function of initial water

722　content. Our results indicate that increasing the amount of $H_2O$ in the system leads to

723　a decrease of feldspar modal amount (**Fig.12b**; see also Green, 1982). Given the

724　apparent scarcity of feldspar within amphibolite to HP-granulite-facies assemblages

725　(between 5 and 15 vol.%; e.g. **Fig.3a**), we believe that an amount of 3 wt.% $H_2O$ is a

726　reasonable estimate for calculating a P-T grid for this bulk composition. The result of

727　this calculation for a fixed amount of 3% $H_2O$ is shown in **figure 12c**. The P-T field

728　obtained for peak metamorphic conditions is in agreement with peak P-T estimates

729　yielded by conventional thermobarometric methods (see section 6.1). These

730    calculations imply that a fluid infiltrated the Lazaro unit during peak metamorphism

731    and this triggered partial melting close to the solidus. At this stage under fluid flux,

732    hornblende is stable at near 750 °C, but was partially consumed to form diopside,

733    garnet and melt (**Fig.12d**). This statement is in agreement with petrological

734    observations demonstrating the amphibole has not been completely consumed at the

735    time of partial melting at peak T (e.g. **Fig.3f**). The calculated $Na_B$ content of peak

736    amphibole at 750°C and 1.2 GPa is 0.25 a.p.f.u., in agreement with EMP data (**Table**

737    **1; Fig.5**). The calculations presented here show that both amphibole and epidote

738    were the hydrous phases involved in melting reactions, in agreement with natural and

739    experimental observations at pressures higher than 1.0 GPa (e.g. Vielzeuf and

740    Schmidt, 2001; García-Casco et al., 2008). On the other hand, the presence of

741    hornblende and feldspar in the peak metamorphic assemblage indicates that

742    temperature never exceeded ca. 790°C (**Figs.12c** and **12d**).

743

744 **Figure 12**: Pseudosection modeling results performed on a MORB composition in the
745    NCKFMASH system using the software Perplex. **a**. T-[$H_2O$] pseudosection calculated at 1.2
746    GPa for a MORB composition showing theoretical phase assemblages in the best-fit region
747    (determined using conventional thermobarometry; see text). The HT-limit of the best-fit
748    region is based on Fsp disappearance. The bulk composition (in wt.%) used for the modeling
749    is the following: $SiO_2$(50.9)$Al_2O_3$(14.5)FeO(10.8)MgO(8)CaO(10.95)$Na_2O$(2.78)$K_2O$(0.16). **b**.
750    Modal evolution of mineral abundances near peak conditions calculated along the path
751    depicted in figure a (grey arrow). The observation of coeval garnet, diopside, amphibole, melt
752    and feldspar (<10 vol.%) in best-preserved samples (e.g. #25) suggests that around 3 wt.%
753    of water was present during melting in the best-fit P-T window. **c**. P-T pseudosection
754    calculated using 3 wt.% free $H_2O$ and the same MORB composition. The transparent box
755    corresponds to the best-fit range based on conventional thermo-barometric approach (see
756    text). The grey arrow corresponds to the hypothetical prograde P-T gradient assumed for
757    Lazaro unit HP rocks. Given the mobility of the fluid phase and the opening of the system, we
758    emphasize that this diagram is only shown as an indication since the location of the fields
759    depends on the amount of fluid in the system which can substantially vary a function of fluid

influx and melt extraction. Note that the unexpected presence of melt in the upper left corner
of the pseudosection may arise from the use of a haplogranitic melt model for this mafic bulk
composition. **d**. Modal evolution of mineral abundances near peak conditions calculated
along the prograde path localized in figure 12c. The best-fit P-T range corresponds to the
box shown in figure c. Calculated mineral compositions are shown for comparison to mineral
EPM analyses.
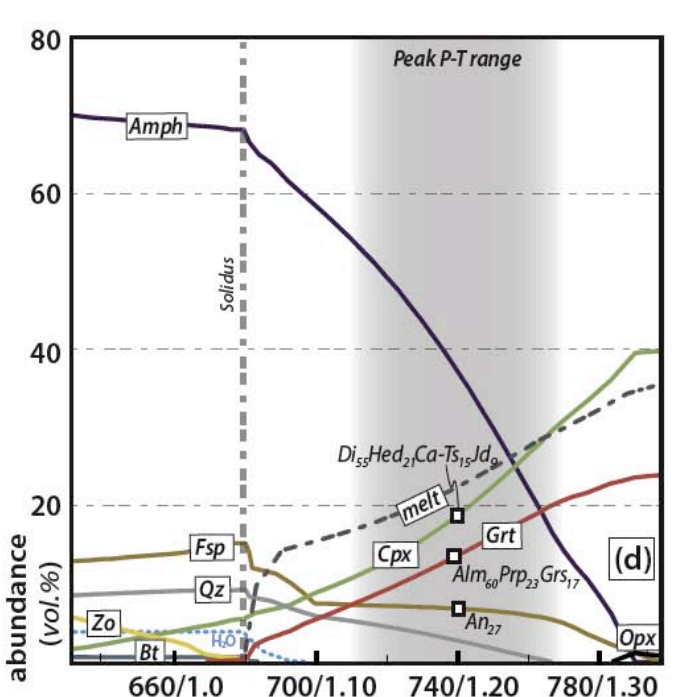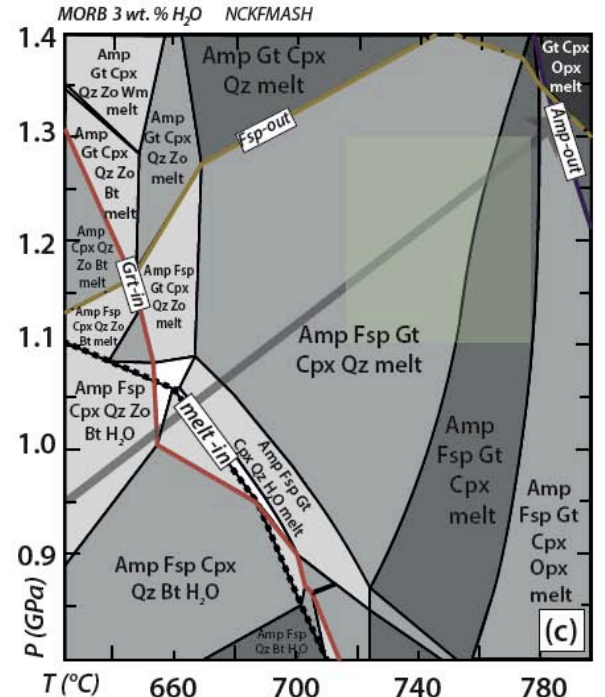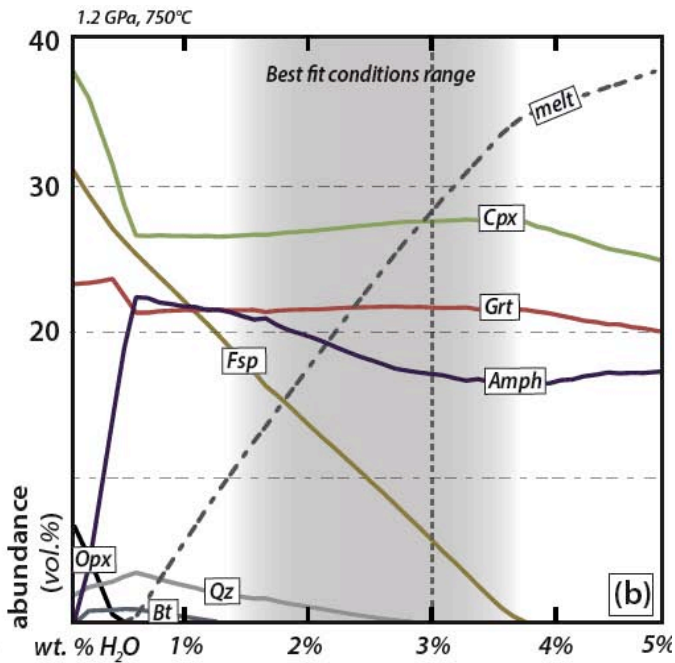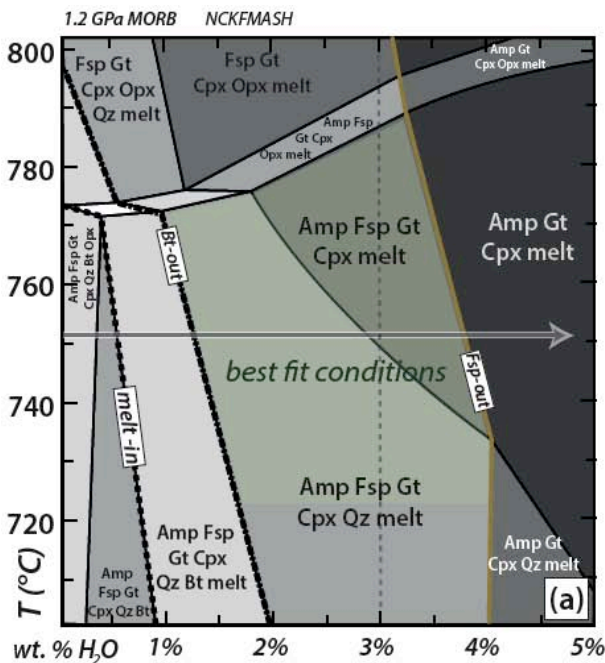
## 6.4    Average P-T

Additional P-T calculations have been carried out using the multi-equilibrium thermobarometric approach. Optimal thermobarometry (Powell and Holland, 1994) was performed using the software THERMOCALC (Holland and Powell, 1998, version 3.33). End member activities and their uncertainties were calculated with the software AX (Holland, unpublished). Calculations were performed with a pure $H_2O$-fluid.

Due to large error bars obtained with average P-T calculations, we fixed the temperature to evaluate pressure during peak T metamorphism. We calculated the average-P for a temperature series between 650 °C and 850 °C with 25°C steps on sample #25 (epidote-clinopyroxene-hornblende-garnet-quartz), which resulted in a pressure  of 1.37 GPa (sd = 0.314 GPa, fit = 0.71 < $1.61_{sigfit}$). This P estimate yields a P range in agreement with the results from the other methods presented above.


## 7.   GEOCHRONOLOGY

### 7.1 Rb-Sr geochronology

The Rb-Sr internal mineral isochron approach is particularly well suited for dating ductile deformation events in white-mica bearing metamorphic rocks. Deformation-induced recrystallization and re-equilibration of mineral phases (such as white mica, albite, apatite and titanite) leads to complete Sr-isotopic re-equilibration and reset of ages under moderate and high temperature (Inger and Cliff, 1994). Isotopic inheritance due to incomplete resetting of the pre-deformation isotopic

793  system may lead to isochron patterns showing partial disequilibrium (e.g. Angiboust

794  et al., 2014). We analyzed different grain-size fractions in order to (i) better evaluate

795  the importance of incomplete resetting of white mica isotopic composition and (ii)

796  detect potentially protracted recrystallization or deformation histories of the studied

797  rocks. This approach generally yields younger apparent ages for smaller grain-size

798  white mica fractions (Angiboust et al., 2014). Thus, younger apparent ages

799  calculated using small grain-size mica fraction can be considered as maximum age

800  estimates for the end of ductile deformation. For Rb-Sr dating of the tectonic

801  overprint we selected samples with pervasive, fine-grained mylonitic foliation and

802  devoid of porphyroclasts in order to avoid isotopic relics.

803      Three metasedimentary samples from the Lazaro unit showing white-mica

804  bearing mylonitic deformation were processed for multi-mineral Rb-Sr geochronology

805  in order to constrain the timing of the LT tectonic overprint reported here (stage 2;

806  complete dataset available in **Electronic Appendix 3**). The three datasets obtained

807  here show variable degrees of isotopic disequilibrium confirming microtextural

808  evidence that indicates multi-stage deformation events (see section 6; **Fig.13**).

809  Sample #24 (metasedimentary rock), showing large muscovite crystals rimmed by

810  phengite, exhibits disequilibrium textures and ages (as expected from micro-chemical

811  mica zoning imaging; **Figs.9a** and **13a**). An age calculation attempt using the

812  smallest analyzed muscovite fraction (160-125µm) and apatite leads to a maximum

813  age for the end of deformation at 116.3 ± 1.8 Ma. Similar disequilibrium has been

814  obtained for sample #23-b3 (**Fig.13c**). The age of 83.1 ± 1.4 Ma, calculated using the

815  smallest analyzed phengite fraction and albite-quartz aggregates, is considered to be

816  a reliable estimate for the maximum age for the end of LT deformation. An age of

41

817    94.6 ± 7.2 Ma has been calculated for sample #29a, a LT-mylonite located on the

818    contact between the Lazaro unit and the Almagro blueschist complex (Puerto shear

819    zone; **Fig.1c**). The 116.3 Ma age for sample #24 was obtained from muscovite that

820    formed by replacement of stage 1 K-feldspar during cooling (**Fig.9a**). This age is

821    clearly older than the two other younger ages of 82-85 Ma and 87-101 Ma

822    (respectively samples #23b3 and #29a), calculated using phengite crystals from the

823    mylonitic foliation (and not muscovite as for #24). This distribution therefore shows

824    that Lazaro unit rocks underwent at least two stages of tectonic overprint between c.

825    120 Ma and c. 80 Ma leading to incomplete re-equilibration that yields the large age

826    spread for end-of-deformation estimates.

827

828    **7.2    Sm-Nd geochronology**

829    In order to constrain the age of peak T metamorphism, we processed two

830    samples: a garnet megablast-bearing sample (#26b; **Fig.3d**) and a garnet-bearing

831    melanosome (sample #25; **Fig.3a**). Petrological investigations have shown that these

832    garnet crystals are only made of Grt 1 generation and are only barely zoned. The

833    isochron shown in **figure 13d,** calculated combining two fractions of garnet

834    fragments, the whole rock and the apatite crystals (see **figure 4d**) yielded a precise

835    isochron age of 163.7 ± 2.1 Ma. This age is consistent with 163 ± 18 Ma derived for

836    granulite-facies sample #25 using different garnet fractions, titanite, apatite,

837    hornblende and feldspar (**Fig.13e**). The large uncertainty associated with this age is

838    due to the low spread between $^{147}Sm/^{144}Nd$ ratios in the analyzed mineral fractions

839    (see complete dataset in **Electronic Appendix 3**).

840

841
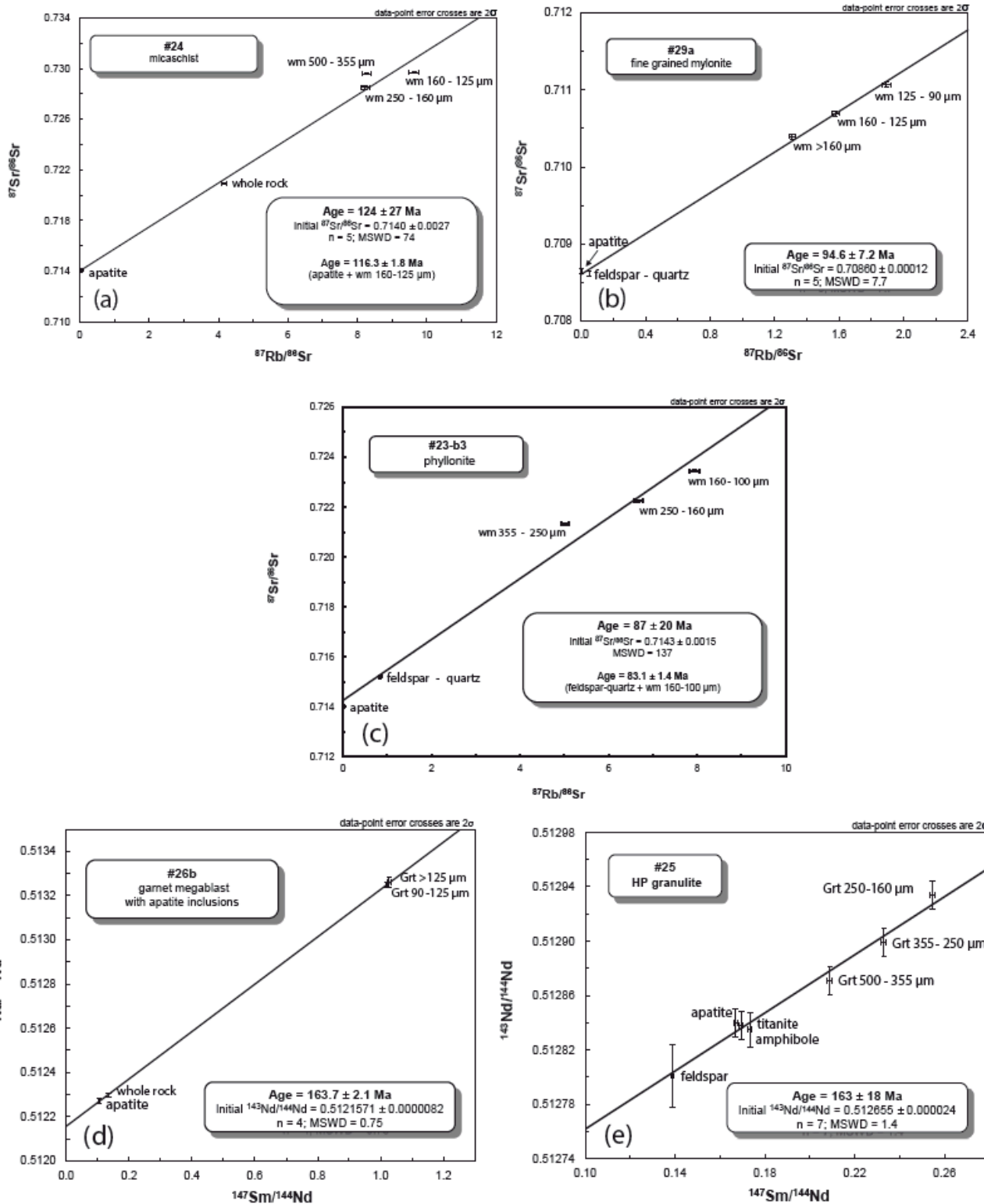
**Figure 13**: Geochronological results using Rb-Sr (**a, b, c**) and Sm-Nd (**d, e**) techniques

843

### 7.3 Zircon U-Pb geochronology

845 SHRIMP U-Th-Pb results are presented in **Figure 14** and the complete

846 analytical dataset given in **Electronic Appendix 4**. Metasedimentary sample #24

847 contains zircon with a wide range of sizes and morphologies, as expected for

848 metasedimentary zircon. In this sample we measured 71 spots, 62 of which yielded

849 concordant ages (discordance ≤±5 %). The ages obtained may be divided into three

850 groups.

851 The first group consists of Precambrian zircons with colorless rounded cores and

852 rare rims, with a size of up to 125 μm x 50 μm. Under the electron microscope most

853 grains show bright cathodoluminescence (CL) signals and oscillatory zoning (**Fig.**

854 **14a**). Eight U-Th-Pb measurements on 6 zircon grains yielded concentrations of U in

855 the range 71-827 μg/g and Th in the range 14-177 μg/g with Th/U ≈ 0.02-0.75 (**Fig.**

856 **14d**). They do not contain common lead (f206 ≈ -0.01 to 0.38 %) and are concordant

857 (discordance ≈ -3.4 to 2.4 %). The $^{206}$Pb/$^{238}$U age comprises two Mesoproterozoic,

858 1277-1062 Ma, one Neoproterozoic (Tonian), 723 ± 40 Ma, one Neoproterozoic

859 (Cryogenian), 678 ± 30 Ma, and four Neoproterozoic (Ediacaran), 629-552 Ma,

860 zircons (**Electronic Appendix 4** and **Fig. 14b**).

861 The second group is of Paleozoic-Triassic age and is made of stubby medium-sized

862 cores, 75 μm x 50 μm, with oscillatory zoning, irregular terminations and bright CL

863 signals (**Fig.14a**). Twenty-five U-Th-Pb measurements on 25 zircon grains yielded

864 high concentrations of U (124-1132 μg/g) and Th (15-630 μg/g) with Th/U ≈ 0.02-1.8

865 (**Fig. 14d**). They contain small amounts of common lead (f206 ≈ -0.22 to 0.54 %) and

866 all are concordant (discordance ≈ -0.8 to 3.4 %). The $^{206}$Pb/$^{238}$U age comprises two

867 Cambrian, 524-495 Ma, three Ordovician, 472-455 Ma, one Silurian, 431 ± 6 Ma,

868    three Devonian, 414-360 Ma, two Carboniferous, 350 ± 5 Ma and 320± 5 Ma, and

869    fourteen Permian, 298-266 Ma, zircons (**Electronic Appendix 4** and **Fig.14b**). This

870    298-266 Ma core age group represents a prevalent age signal in the sedimentary

871    zircon record. Two zircon grains show highly luminescent cores, 100 µm x 50 µm,

872    with Triassic $^{206}$Pb/$^{238}$U ages of 251-250 Ma (**Fig.14a**).
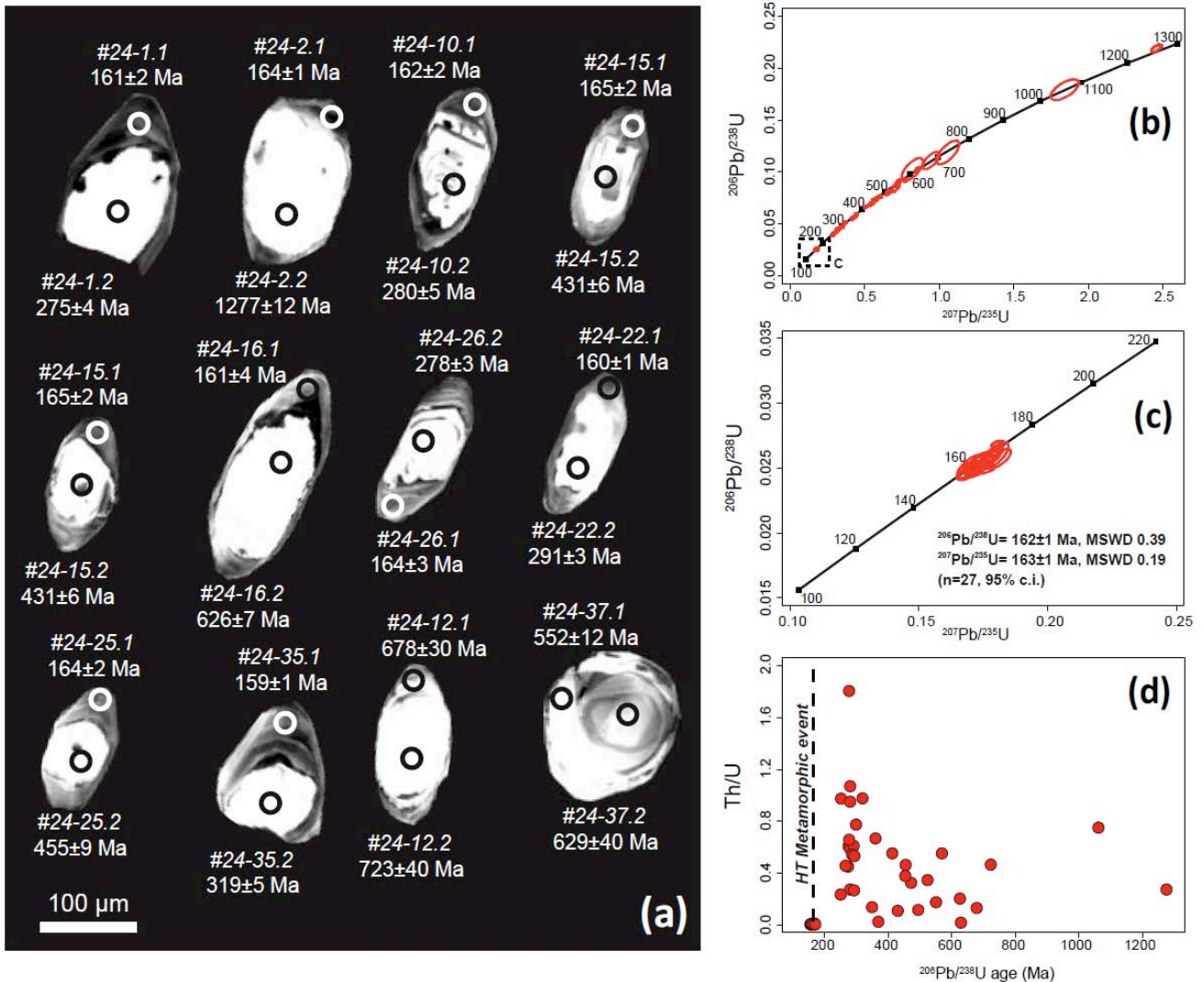


873

874    **Figure 14**: Results from the U-Th-Pb zircon dating. **a.** Cathodoluminescence images and
875    $^{206}$Pb/$^{238}$U ages of representative analysed zircon grains from the metasedimentary rock #24.
876    Note that all low cathodoluminescence overgrowths on older grains yield an age c. 162 Ma.
877    Note also the evidence for dissolution of numerous zircon cores during the stage 1 HT event.
878    **b**. Wetherill concordia plot for sample #24. **c**. Wetherill Concordia detail for low CL signal

45

879     rims. **d**. Zircon Th/U ratio vs $^{206}$Pb/$^{238}$U ages, note the lowest Th/U values of low CL signal, c

880     162 Ma, rims.

881

882     The third group is Middle-Late Jurassic (Callovian-Oxfordian) and comprises small

883     (60 µm x 30 µm), dark cathodoluminescence rims overgrowing all zircons in the

884     sample, independent of their age (**Fig.14a**). Some of these rims also show oscillatory

885     zoning (**Fig.14a**). Twenty-seven of these rims contain high concentrations of U (751-

886     1604 µg/g) and low Th (6-15 µg/g), with the lowest Th/U ≈ 0.006-0.01, combined with

887     only small proportions of common lead (f206 < 0.34 %). All of them are concordant

888     (discordance ≈ -1.4 to 3.2 %). The weighted mean (errors reported at 2σ) of the

889     uncorrected $^{206}$Pb/$^{238}$U ages, 162 ± 1 Ma (MSWD = 0.39), is virtually identical to the

890     $^{207}$Pb/$^{235}$U age of 163 ± 1 Ma (MSWD = 0.19; **Electronic Appendix 4** and **Fig.14c**).

891

892     **8.    DISCUSSION**

893         **8.1     Pressure-Temperature-time history of Lazaro unit**

894

895         Lazaro unit rocks reveal a two-fold tectono-metamorphic history visible in the

896     structural record in the field and in the mineral zoning patterns. The prograde, burial

897     history has not been preserved due to the high temperature of peak metamorphism

898     and a long-term re-equilibration during cooling and exhumation (see also Willner et

899     al., 2004b). Our P-T estimates show that peak metamorphic conditions reached c.

900     1.2 GPa and 750°C (~40 km depth using an integrated rock density of 3) at the

901     transition from the albite amphibolite facies to the HP granulite fields (O'Brien and

902     Rötzler, 2003). This metamorphic event led to the formation of variable amounts of

903     melt due to hydrous fluid influx and to the crystallization of a large amount of

904     peritectic garnet associated with garnet-bearing melanosomes. Some of these HT

garnet crystals preserve oriented ilmenite and rutile exsolution needles, which are typical features of HT/HP and UHT terranes worldwide (**Fig.4c**; e.g. Snoeyenbos et al., 1995; Ague and Eckert, 2012). Rounded, poly-mineralic inclusions in garnet also recall the texture of melt inclusions ("nanogranites") increasingly reported in migmatitic and granulitic terranes worldwide (**Fig.4g**; Cesare et al., 2009). Some samples (e.g. #25a; **Fig.6b**) exhibit myrmekite-like intergrowths of epidote and quartz spatially associated with peritectic garnet in melanosomes. Such texture has been observed in magmatic, migmatitic and pegmatitic rocks and interpreted to have formed by the crystallization of phases from a silicate melt at pressures exceeding 0.8 GPa in the presence of a hydrous fluid (Zen and Hammarstrom, 1984 and references therein; Jones and Escher, 2002). The absence of this magmatic epidote in some samples may be related to local $H_2O$-undersaturation during the stage 1 event or, more likely, to insufficient pressure. The latter could indicate that these rocks stayed just in the limit of the "epidote-in" reactions, at c. 1.2 to 1.3 GPa (e.g. García-Casco, 2007), which may have precluded the formation of epidote from some bulk compositions.

The SHRIMP U-Th-Pb zircon rims from the metasedimentary rock sample #24 yield near-peak metamorphic ages of c.161-164 Ma around detrital grains, in good agreement with multimineral Sm-Nd ages of samples containing peritectic garnet (163 ± 2 Ma and 163 ± 18 Ma; **Figs.13d, 13e** and **14**). Altogether our results demonstrate that peak metamorphic conditions were reached at around 163 Ma at c. 40 km depth in a hot subduction environment (c. 19 °C/km). U-Th-Pb zircon rim ages of 160-175 Ma obtained by Hervé and Fanning (2003) on siliceous gneisses from the Lazaro unit were interpreted as related to acidic magmatism during extension of the

upper continental crust (Gondwanaland). We believe, instead, that these ages, which

overlap our range, reflect zircon growth associated with the crystallization of the melt

at the deep subduction interface. Temperature estimates (~750°C) obtained for

garnet amphibolite, combined with the finding of magmatic epidote and

pseudomorphs after K-feldspar, confirms that metasedimentary rocks also underwent

anatexis. Partial melting processes in felsic rocks triggers zircon dissolution and its

subsequent precipitation during melt crystallization (Rubatto et al., 2009 and Kohn et

al., 2015). Our cathodoluminescence images of zircons, together with those shown

by Hervé and Fanning (2003), confirm that dissolution of detrital zircon cores most

likely took place during stage 1 and associated melt production.

As also noticed by Hervé and Fanning (2003) and Willner et al. (2004a), Lazaro unit

rocks have been massively affected by cooling-related metamorphic recrystallization

and deformation. The stage 2 LT metamorphic event overprinting Lazaro unit rocks is

characterized by growth of blue Na-rich hornblende rims around brown peak T

amphibole, the formation of Si-rich phengite rims around muscovite and the

pervasive replacement of garnet by chlorite. Chlorite-phengite P-T estimates show

that cooling took place between 0.9 and 1.3 GPa. The formation of Si-rich phengite

rims around muscovite flakes is in agreement with isobaric cooling down to 450-

500°C under epidote-blueschist facies conditions before decompression and

exhumation (**Fig.15**). Even though some uncertainty exists on the pressure

experienced by the Lazaro unit throughout the cooling process, no significant vertical

displacement can be inferred from the petrological record. In particular, the absence

of orthopyroxene confirms that these rocks have not undergone near-isothermal

decompression after peak metamorphism (e.g. Pattison, 2003).

953 An interesting feature is the observation of a low XMg garnet generation (Grt2)

954 overgrowing the HT garnet and sealed fracture networks (**Fig.7b**). Since the growth

955 of garnet is hampered by cooling (**Fig 12**), we postulate here that the pattern visible

956 in **Figure 7b** indicates (i) fracturing, breakdown and chloritization of garnet during

957 cooling at HP (ii) short-lived warming up and healing of garnet fractures, and (iii) later

958 cooling, fracturing and replacement by chlorite along new fracture networks. This

959 episode of heating may be correlated with the short-lived increase of the thermal

960 gradient from 10 to 13°/km associated with amphibolitization of the underlying

961 Almagro blueschist complex at c. 120 Ma reported by Hyppolito et al. (2016).
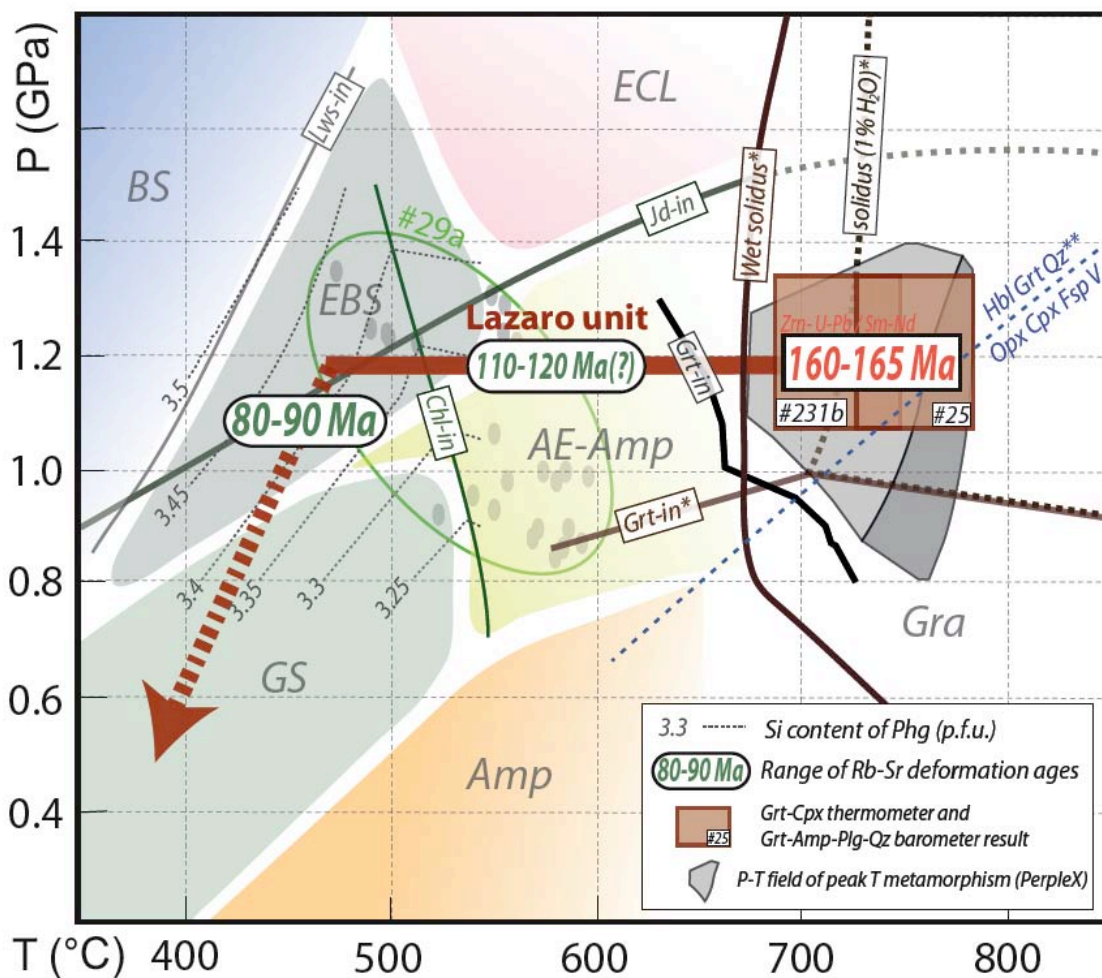


962

963 **Figure 15**: Pressure-Temperature-time diagram showing the counterclockwise evolution of

964 the Lazaro unit between 162 and 80 Ma. The garnet-in and the solidus curves are from

965 Vielzeuf and Schmidt (2001). The (**) curve corresponding to the disappearance of

966 orthopyroxene is from Pattison (2003). The grey-shaded domains in the peak T region

967 correspond to the best-fit assemblage fields calculated using pseudosection modeling (figure

968 12). The red boxes correspond to P-T estimates based on conventional thermobarometry for

969 samples #2-31b and #25 (see text and Table 3). The green circle corresponds to the best-fit

970 ellipse for Chl-Phg P-T estimates for the LT-mylonite #29a (see Electronic Appendix 2 for

971 details). The isopleths of the Si-contents in phengite (and the chlorite-in curve) in the epidote

972 blueschist facies has been calculated using the bulk composition of sample #25 and a set of

973 activity models similar to those used in Angiboust et al. (2014). The background

974 metamorphic grid is modified after Evans (1990).

975

976 Isotopic disequilibrium in Rb-Sr geochronological results independently confirms that

977 the pervasive (but incomplete) retrogression of the Lazaro unit was a long-lasting

978 process that took place over ca. 40 Myr between 120 and 80 Ma. Our oldest Rb-Sr

979 age of 124 ± 27 Ma is close to the age of 117 ± 28 Ma obtained by Willner et al.

980 (2004a) on a Lazaro unit orthogneiss (DA37) using K-Ar on amphibole and

981 interpreted as a cooling age after HT metamorphism. These two ages suggest that

982 the T range 550-600°C (i.e. the assumed closure T range for K-Ar in amphibole; Villa,

983 1998) has been crossed at around c.120 Ma during cooling in the subduction zone

984 environment (**Fig.15**). This temperature range coincides with peak-temperatures

985 (550-600°C) estimated by Willner et al. (2004) for garnet amphibolite samples buried

986 along a prograde metamorphic path. These garnet amphibolites (together with some

987 retro-eclogites amphibolitized at 120 Ma from Hyppolito et al., 2016) are now

988 exposed in the footwall of the Lazaro unit along the Puerto shear zone (Fig.1c). This

989 observation suggests that the Lazaro unit and the underlying garnet amphibolites

990 from the Almagro complex probably shared a common tectono-metamorphic history

991 since their juxtaposition at c. 120 Ma.

992 Last, the static sub-silicic pargasite forming over the garnet amphibolite fabric

993 (**Electronic Appendix 1**; see also Willner et al., 2012 for the Choapa complex in

994 central Chile) may be related to a later warming event, such as the emplacement of a

995 magmatic intrusion affecting shallow levels of the wedge (< 0.4 GPa), linked to the

996 South Patagonian Batholith (e.g. Hervé et al., 2007).


997

998 **8.2    Evidence for partial melting of oceanic crust**

999

1000 Natural occurrences exposing vestiges of subduction-related melting of oceanic crust

1001 are rare on Earth (e.g. Cuba: Garcia-Casco et al., 2008; Catalina Schists: Sorensen

1002 and Barton, 1987; Iran: Rossetti et al., 2010). Our results provide insight on the

1003 nature of the material that experienced melting during subduction. Bulk and trace

1004 element geochemical results clearly point to MORB signatures largely similar to the

1005 underlying Almagro Complex rocks (**Fig.11**). The low Zr content of the trondhjemitic

1006 sample #25b (14 µg/g; **Table 2**) corroborates its derivation from MORB-like rocks.

1007 This also confirms that hornblende and rutile retain Zr during prograde

1008 metamorphism and melt production in mafic rocks (Kohn et al., 2015). The finding of

1009 a phengite-quartz metasedimentary rock (#24) with a detrital zircon population with

1010 ages between 1200 Ma and 280 Ma (**Fig.14**) indicates that metasedimentary lenses

1011 were interleaved with mafic lithologies in the Lazaro unit. The detrital zircon pattern

1012 shows a noticeable Permian peak which is similar to those recognized in sandstones

1013 and greywackes of the Madre de Dios Accretionary Complex (MDAC; **Fig.1**; Hervé et

1014 al., 2003; see also Castillo et al., 2016). We do not consider these micaceous schists

1015 to derive from an upper plate granite (as proposed by Hervé and Fanning, 2003) but

1016 rather from metasedimentary rocks. In addition, the preservation of thin spessartine

1017 quartzite bands interleaved with amphibolites (**Fig.3e**) supports the idea that Lazaro

1018 unit rocks correspond to a tectonic slice of ocean-floor affinity. The formation of

1019 trondhjemitic leucosomes is also a reliable indication supporting partial melting of

1020 mafic material (**Fig.10**; see also Rapp et al., 1991 and Blanco-Quintero et al., 2011).

1021 Field investigations revealed the existence of hornblende-rich amphibolites within the

1022 Lazaro unit (**Fig.3**). Phase relationships and trace element patterns (**Figs.10** and **11**)

1023 have shown that some of these rocks underwent melt extraction as shown by the

1024 residual geochemical signature of some samples ("picrites"; see also **Fig.11a**). The

1025 large garnet crystals, however, are due to abundant water influx (**Fig.2d**) confirming

1026 the residual nature of these garnet amphibolites and suggesting melt loss during

1027 stage 1 metamorphism (see also Powell and Downes, 1990). Petrological

1028 relationships and pseudosection modeling confirm that an aqueous fluid infiltrated

1029 during, and triggered, the melting process. The formation of a garnet-hornblende-

1030 bearing residue also suggests that melting proceeded before dehydration of prograde

1031 amphibolite (**Figs.3c,f**; Drummond and Defant, 1990; Foley et al., 2002). The

1032 presence of 2 to 4 wt.% $H_2O$ during the melting process (see **Fig.12**) implies a

1033 contribution from external fluids since (i) high grade mafic rocks do not generally

1034 contain more than 1.6 wt.% $H_2O$ (Clemens and Vielzeuf, 1987), and (ii) free fluids are

1035 needed to enable the formation of a Na-rich melt such as a trondhjemitic melt

1036 (Prouteau et al., 2001).

1037 Hornblende-rich amphibolites and the associated garnetite domains correspond to

1038 residual solid phases and shed light on melt extraction in subduction environments

1039 (**Figs. 2c and 3**; Wolf and Wyllie, 1993; Sawyer, 2014). Positive volume change

1040 during melt production is known to lead to embrittlement and micro-fracturing (e.g.

1041 Connolly et al., 1997; see field evidence for micro-cracking in **Electronic Appendix**

1042 **1**). Local melt may have collected along HT shear zones enabling melt extraction and

1043 leaving a garnetite behind (Brown, 2004). Similar garnetite has been reported by

1044 Daczko et al. (2001) in high-pressure granulites (750°C, 1.4 GPa) from the Fjordland

1045 region (New Zealand) and by Yamamoto and Yoshino (1998) for the Jilal complex in

1046 the Kohistan arc (735-949°C, 1.0-1.7 GPa). The generated melt escaped along these

1047 Grt-bearing restites and migrated upwards towards shallower magmatic reservoirs

1048 feeding andesitic and adakitic volcanoes (e.g. Condie, 2005; Martin et al., 2005).

1049 Therefore the Lazaro unit constitutes an interesting field analogue highlighting the

1050 nature of the source material producing Tonalitic-Trondhjemitic-Granodioritic suites

1051 (TTG) in Phanerozoic subduction zones.

1052

1053     **8.3    A hot subduction during the Jurassic**

1054

1055 The partial melting of the Lazaro unit took place along an 18-20°C/km prograde

1056 thermal gradient (**Fig.15**). Such a gradient is much warmer than the one proposed for

1057 "normal" warm, present-day subduction zones where young oceanic lithosphere

1058 subducts (e.g. SW Japan: around 12°/km; Peacock and Wang, 1999). It is known

1059 that the entrance of very young oceanic lithosphere into the mantle shortly after

1060 subduction initiation can lead to very high metamorphic gradients and temperatures

1061 as high as 800°C at 40 km depth along the interface (Defant and Drummond, 1990;

1062 Peacock, 1991; Nikolaeva et al., 2010). Numerical models confirm that after

1063 subduction initiation (typically 4-5 Ma; see **Electronic Appendix 5**) of an oceanic

1064 plate with a thermal age of 3 Ma, only a few millions of years are needed to reach a

1065 prograde thermal gradient of 18-20°/km. However, in the case of the south central

1066 Chile and Patagonia it is likely that subduction along the SW margin of the

1067 Gondwana continent had already started in Paleozoic times (Glodny et al., 2005;

1068 Charrier et al., 2007; Willner et al., 2009; Hervé et al., 2013).

1069 The fragmentation of the Gondwana supercontinent between middle Triassic and

1070 early Cretaceous times was characterized by an alternation of extensional regimes

1071 with subduction rate decrease and/or cessation (e.g. Gorczyk et al., 2007; Charrier et

1072 al., 2007) and synchronous extension and subduction (e.g. Stern and De Wit, 2003;

1073 Mpodozis & Ramos, 2008). Between ca. 170 and 150 Ma, extension-related

1074 intracontinental volcanic deposits covered a great part of austral Patagonia coeval

1075 with the opening of the Weddell Sea and the incipient drifting of the Antarctica

1076 Peninsula to the south (Ghidella et al., 2002; Pankhurst et al., 2000; Hervé &

1077 Fanning, 2003; Jokat et al., 2003). Our new data, in line with these models, confirm

1078 that the drift of the Antarctica Peninsula to the south, closely associated with the

1079 opening of the Weddell sea (Ghidella et al., 2002; Mpodozis & Ramos, 2008), started

1080 in the middle/late Jurassic. We hypothesize that the Lazaro unit rocks constitute

1081 remnants from hot oceanic subduction subsequently developed along the

1082 southwestern Gondwana margin in a regionally extensional regime. This late

1083 Jurassic subduction event correlates with the onset of magmatism in the forearc at c.

1084 160 Ma when the Patagonian Batholith started to form (Hervé et al., 2007; Parada et

1085 al., 2007). An analogue of this process has been described by Kay et al. (2004) in the

1086 triple junction region (c. 49°S) where c. 12 Ma slab-melt adakites are related to the

1087 partial melting of the young and hot subducting Nazca plate (Patagonian Cordillera,

1088 Cerro Pampa). Similarly, it has been demonstrated that the SW Japanese margin

1089 evolved from a transform to a hot subduction margin over the last 30 Ma, leading to

the generation of adakitic volcanoes and extension in the upper plate (e.g. Kimura et al., 2005 and references therein).

### 8.4 Regional implications and open questions

Diego de Almagro Island constitutes a valuable and (nearly) unique witness documenting the nature and dynamics of the South Chilean subduction zone during Mesozoic times. First, we have shown that the Lazaro unit records an early stage of accretion of hot and young oceanic crust that proceeded at c. 40 km depth along the interface (see also similar observations in E. Cuba; Blanco-Quintero et al., 2011 and Catalina island: Sorensen and Barton, 1987). Our P-T-t reconstruction suggests that the Lazaro unit (i) remained at around 40 km depth, after accretion along the hanging wall of the subduction channel, for more than 80 Ma (**Fig.15**), and (ii) recorded the long-term thermal evolution of the Patagonian subduction zone. The time gap (160-120-80 Ma) existing between the various accreted elements on Diego de Almagro Island indicates transient episodes of underplating throughout the tectonic history of the island (e.g. Platt et al., 1986; Angiboust et al., 2016).

Yet, episodes of tectonic erosion of the upper plate may have preceded or co-existed with this accretionary regime. It is striking to note the similarities between the Madre de Dios basin ages (c. 270 Ma for the youngest detrital zircons; Hervé and Fanning, 2003; Sepulveda et al., 2010; **Fig.1c**) and a marked age cluster at 270-290 Ma found in zircon cores from mica schist sample #24. From this perspective, the Lazaro unit may represent a coherent fragment of the Madre de Dios accretionary wedge consumed by tectonic erosion slightly before c. 160 Ma, followed by accretion at c. 40km depth (see also Hervé and Fanning, 2003 and Angiboust et al., 2014).

Another similarity with previous work lies further south in the Cordillera Darwin where medium to high grade (0.9-1.2 GPa, ~620°C) Cretaceous rocks have been described (~90 Ma to 65 Ma, $^{40}$Ar-$^{39}$Ar cooling mica ages and U-Th-Pb on monazite; Kohn et al., 1995 and Maloney et al., 2011). Interestingly, a Jurassic Rb-Sr whole rock isochron age of 157 ± 7 Ma (Hervé et al., 1981) and an U-Pb zircon age of 164 ±1 Ma (Mukasa and Dalziel, 1996) were obtained on a peraluminous orthogneiss from the Cordillera Darwin. It remains uncertain whether these rocks and the Lazaro unit on Diego de Almagro Island were formerly part of the same tectonic element during middle to late Mesozoic deformation along the Patagonian margin. Future investigations should help to (i) better understand the tectonic origin of the protoliths and the genesis of this cordillera and (ii) reconstruct the location of the Jurassic plate boundary and the paleogeographic link between Darwin Cordillera, Diego de Almagro and Diego Ramirez Islands (e.g. Kohn et al., 1995; Hervé et al., 2008).

Finally, the significance of the Seno Arcabuz Shear Zone, which delimits the Lazaro unit to the east, remains unclear (**Fig.1c**). The fact that this shear zone was undergoing LP-HT deformation (< 0.6 GPa, 500-600°C; Willner et al., 2004) at c. 120 Ma while the Lazaro unit was still at HP conditions (c. 1.2 GPa; this work) needs clarification. An understanding of the evolution and significance of the Seno Arcabuz Shear Zone will be an important research target in the future as it may represent the former plate boundary prior to accretion of the Lazaro unit to the Gondwana margin.


**9. CONCLUSIONS**

Evidence for partial melting of subducted oceanic crust has been discovered in the Lazaro unit (Diego de Almagro Island). Thermobarometric results show that wet melting took place at around 1.2 GPa and c. 750°C, leading to the formation of trondhjemitic melts and peritectic garnet. U-Pb dating of zircon rims and Sm-Nd geochronology on garnet-bearing HP granulite-facies assemblages reveal an age of c. 162 ± 2 Ma for this HT event. Combined with other ages showing that emplacement of the Patagonian batholith started at c. 160 Ma, we propose that the high temperature metamorphic overprint visible in the Lazaro unit records a stage of subduction of a hot and young oceanic plate along the W margin of the Gondwana continent coeval with regional extension after a period of quiescence during the Triassic. Our results also suggest that the Lazaro unit remained along the subduction interface from c. 165 Ma to 80 Ma. This long-lasting residence time explains the pervasive retrogression during isobaric cooling through epidote amphibolite and upper greenschist-facies conditions. The record of long-term deformation on Diego de Almagro Island constitutes a valuable witness to a better understanding of the structural and thermal evolution of the roots of the Chilean accretionary system from Jurassic to upper Cretaceous times.

1168

## REFERENCES

Ague, J. J., & Eckert, J. O. (2012). Precipitation of rutile and ilmenite needles in garnet: Implications for extreme metamorphic conditions in the Acadian Orogen, USA. American Mineralogist, 97(5-6), 840-855.

Angiboust, S., Glodny, J., Oncken, O., and Chopin, C. (2014). In search of transient subduction interfaces in the Dent Blanche–Sesia Tectonic System (W. Alps). Lithos, 205, 298-321.

Angiboust, S., Agard, P., Glodny, J., Omrani, J., & Oncken, O. (2016). Zagros blueschists: Episodic underplating and long-lived cooling of a subduction zone. Earth and Planetary Science Letters, 443, 48-58.

Barker, F. (1979). Trondhjemite: definition, environment and hypotheses of origin. Trondhjemites, dacites and related rocks. Elsevier, Amsterdam, 1, 12.

Berman, R. G. (1991). Thermobarometry using multi-equilibrium calculations: a new technique, with petrological applications. Canadian Mineralogist, 29(4), 833-855.

Black, L.P., Kamo, S.L., Allen, C.M., Aleinikoff, J.A., Davis, D.W., Korsch, J.R., Foudolis, C. (2003). TEMORA 1: a new zircon standard for Phanerozoic U-Pb geochonology. Chemical Geology 200, 155-170.

Blanco-Quintero, I. F., García-Casco, A., & Gerya, T. V. (2011). Tectonic blocks in serpentinite mélange (eastern Cuba) reveal large-scale convective flow of the subduction channel. Geology, 39(1), 79-82.

Brown, M. (2004). The mechanism of melt extraction from lower continental crust of orogens. Geological Society of America Special Papers, 389, 35-48.

Calderon, M., Prades, C. F., Herve, F., Avendaño, V., Fanning, C. M., Massonne, H. J., ... & Simonetti, A. (2013). Petrological vestiges of the Late Jurassic-Early Cretaceous transition from rift to back-arc basin in southernmost Chile: New age and geochemical data from the Capitán Aracena, Carlos III, and Tortuga ophiolitic complexes. Geochemical Journal, 47(2), 201-217.

1204

1205 Castillo, P., Fanning, C. M., Hervé, F., & Lacassie, J. P. (2016). Characterisation and
1206     tracing of Permian magmatism in the south-western segment of the Gondwanan
1207     margin; U–Pb age, Lu–Hf and O isotopic compositions of detrital zircons from
1208     metasedimentary complexes of northern Antarctic Peninsula and western
1209     Patagonia. Gondwana Research. 36, 1-13.

1210

1211 Cesare, B., Ferrero, S., Salvioli-Mariani, E., Pedron, D., & Cavallo, A. (2009).
1212     "Nanogranite" and glassy inclusions: The anatectic melt in migmatites and
1213     granulites. Geology, 37(7), 627-630.

1214

1215 Charrier, R., Pinto, L., & Rodríguez, M. P. (2007). Tectonostratigraphic evolution of
1216     the Andean Orogen in Chile. The geology of Chile (Moreno, T.; gibbons, W.;
1217     editors). The geological Society, 21-114.

1218

1219 Claoue-Long, J., Compston, W., Roberts, J., Fanning, C.M., 1995. Two carboniferous
1220     ages: a comparison of SHRIMP zircon dating with conventional zircon ages &
1221     40Ar/39Ar analysis, In Berggren, W.A., Kent, D.V., Aubry, M.P., Hardenbol, J.
1222     (eds). Geochronology, Time Scales & Stratigraphic Correlation. SEPM Special
1223     Publication 54, 1-22.

1224

1225 Clemens, J. D., & Vielzeuf, D. (1987). Constraints on melting and magma production
1226     in the crust. Earth and Planetary Science Letters, 86(2), 287-306.

1227

1228 Condie, K. C. (2005). TTGs and adakites: are they both slab melts? Lithos, 80(1), 33-
1229     44.

1230

1231 Connolly, J. A. D. (2005). Computation of phase equilibria by linear programming: a
1232     tool for geodynamic modeling and its application to subduction zone
1233     decarbonation. Earth and Planetary Science Letters, 236(1), 524-541.

1234

1235 Connolly, J. A. D., Holness, M. B., Rubie, D. C., & Rushmer, T. (1997). Reaction-
1236     induced microcracking: an experimental investigation of a mechanism for
1237     enhancing anatectic melt extraction. Geology, 25(7), 591-594.

1238

1239 Dale, J., Powell, R., White, R. W., Elmer, F. L., & Holland, T. J. B. (2005). A
1240     thermodynamic model for Ca–Na clinoamphiboles in Na2O–CaO–FeO–MgO–
1241     Al2O3–SiO2–H2O–O for petrological calculations. Journal of Metamorphic
1242     Geology, 23(8), 771-791.

1243

1244 Daczko, N. R., Clarke, G. L., & Klepeis, K. A. (2001). Transformation of two-pyroxene
1245     hornblende granulite to garnet granulite involving simultaneous melting and
1246     fracturing of the lower crust, Fiordland, New Zealand. Journal of Metamorphic
1247     Geology, 19(5), 549-562.

1248

1249 Dalziel, I. W. D., Grunow, A. M., Storey, B. C., Garrett, S. W., Herrod, L. D. B., &
1250     Pankhurst, R. J. (1987). Extensional tectonics and the fragmentation of
1251     Gondwanaland. Geological Society, London, Special Publications, 28(1), 433-
1252     441.

Defant, M. J., & Drummond, M. S. (1990). Derivation of some modern arc magmas by melting of young subducted lithosphere. Nature, 347(6294), 662-665.

Drummond, M. S., & Defant, M. J. (1990). A model for trondhjemite-tonalite-dacite genesis and crustal growth via slab melting: Archean to modern comparisons. Journal of Geophysical Research: Solid Earth, 95(B13), 21503-21521.

Dubacq, B., Vidal, O., & De Andrade, V. (2010). Dehydration of dioctahedral aluminous phyllosilicates: thermodynamic modelling and implications for thermobarometric estimates. Contributions to Mineralogy and Petrology, 159(2), 159-174.

Ellis, D. J., & Green, D. H. (1979). An experimental study of the effect of Ca upon garnet-clinopyroxene Fe-Mg exchange equilibria. Contributions to Mineralogy and Petrology, 71(1), 13-22.

Evans, B. W. (1990). Phase relations of epidote-blueschists. Lithos, 25(1), 3-23.

Foley, S., Tiepolo, M., & Vannucci, R. (2002). Growth of early continental crust controlled by melting of amphibolite in subduction zones. Nature, 417(6891), 837-840.

Fuhrman, M. L., & Lindsley, D. H. (1988). Ternary-feldspar modeling and thermometry. American Mineralogist, 73(3-4), 201-215.

García-Casco, A., Lázaro, C., Rojas-Agramonte, Y., Kröner, A., Torres-Roldán, R. L., Núñez, K., ... & Blanco-Quintero, I. (2008). Partial melting and counterclockwise P–T path of subducted oceanic crust (Sierra del Convento mélange, Cuba). Journal of Petrology, 49(1), 129-161.

García-Casco, A. (2007). Magmatic paragonite in trondhjemites from the Sierra del Convento mélange, Cuba. American Mineralogist, 92(7), 1232-1237.

Ghidella, M. E., Yáñez, G., & LaBrecque, J. L. (2002). Revised tectonic implications for the magnetic anomalies of the western Weddell Sea. Tectonophysics, 347(1), 65-86.

Glodny, J., Kühn, A., & Austrheim, H. (2008). Diffusion versus recrystallization processes in Rb–Sr geochronology: isotopic relics in eclogite facies rocks, Western Gneiss Region, Norway. Geochimica et Cosmochimica Acta, 72(2), 506-525.

Glodny, J., Lohrmann, J., Echtler, H., Gräfe, K., Seifert, W., Collao, S., & Figueroa, O. (2005). Internal dynamics of a paleoaccretionary wedge: insights from combined isotope tectonochronology and sandbox modelling of the South-Central Chilean forearc. Earth and Planetary Science Letters, 231(1), 23-39.

1300     Gorczyk, W., Willner, A. P., Gerya, T. V., Connolly, J. A., & Burg, J. P. (2007).
1301         Physical controls of magmatic productivity at Pacific-type convergent margins:
1302         Numerical modelling. Physics of the Earth and Planetary Interiors, 163(1), 209-
1303         232.
1304
1305     Hermann, J., Spandler, C., Hack, A., & Korsakov, A. V. (2006). Aqueous fluids and
1306         hydrous melts in high-pressure and ultra-high pressure rocks: implications for
1307         element transfer in subduction zones. Lithos, 92(3), 399-417.
1308
1309     Hervé, F. (1988). Late Paleozoic subduction and accretion in Southern Chile.
1310         Episodes 11, 183-188.
1311
1312     Hervé, F., Prior, D., López, G., Ramos, V.A., Rapalini, A., Thomson, S., Lacassie,
1313         J.P. and Fanning, M. (1999), Mesozoic blueschists from Diego de Almagro,
1314         southern Chile, II South American Symposium on Isotope Geology, Actas,
1315         (Extended Abstract), p.318-321, Córdoba.
1316
1317     Herve, F., Fanning, C. M., & Pankhurst, R. J. (2003). Detrital zircon age patterns and
1318         provenance of the metamorphic complexes of southern Chile. Journal of South
1319         American Earth Sciences, 16(1), 107-123.
1320
1321     Hervé, F., and Fanning, C. M. (2003). Early Cretaceous subduction of continental
1322         crust at the Diego de Almagro archipelago, southern Chile. Episodes, 26(4), 285-
1323         289.
1324
1325     Hervé, F., Pankhurst, R. J., Fanning, C. M., Calderon, M., Yaxley, G. M. (2007). The
1326         South Patagonian batholith: 150 my of granite magmatism on a plate margin.
1327         Lithos, 97, 373-394.
1328
1329     Hervé, F., Calderón, M., & Faúndez, V. (2008). The metamorphic complexes of the
1330         Patagonian and Fuegian Andes. Geologica Acta, 6(1), 43-53.
1331
1332     Herve, F., Calderón, M., Fanning, C. M., Pankhurst, R. J., & Godoy, E. (2013).
1333         Provenance variations in the Late Paleozoic accretionary complex of central
1334         Chile as indicated by detrital zircons. Gondwana Research, 23(3), 1122-1135.
1335
1336     Holland, T. J. B., & Powell, R. (1998). An internally consistent thermodynamic data
1337         set for phases of petrological interest. Journal of metamorphic Geology, 16(3),
1338         309-343.
1339
1340     Holland, T., Baker, J., & Powell, R. (1998). Mixing properties and activity-composition
1341         relationships of chlorites in the system $MgO-FeO-Al_2O_3-SiO_2-H_2O$. European
1342         Journal of Mineralogy, 395-406.
1343
1344     Hyppolito, T., Angiboust, S., Juliani, C., Glodny, J., Garcia-Casco, A., Calderon, M. &
1345         Chopin, C. 2016. Eclogite-, amphibolite- and blueschist-facies rocks from Diego
1346         de Almagro Island (Patagonia): Episodic accretion and thermal evolution of the
1347         Chilean subduction interface during the Cretaceous.
1348

Hyppolito, T., García-Casco, A., Juliani, C., Meira, V. T., & Hall, C. (2014). Late Paleozoic onset of subduction and exhumation at the western margin of Gondwana (Chilenia Terrane): Counterclockwise P–T paths and timing of metamorphism of deep-seated garnet–mica schist and amphibolite of Punta Sirena, Coastal Accretionary Complex, central Chile (34° S). Lithos, 206, 409-434.

Inger, S., & Cliff, R. A. (1994). Timing of metamorphism in the Tauern Window, Eastern Alps: Rb-Sr ages and fabric formation. Journal of Metamorphic Geology, 12(5), 695-707.

Jokat, W., Boebel, T., König, M., & Meyer, U. (2003). Timing and geometry of early Gondwana breakup. Journal of Geophysical Research: Solid Earth, 108(B9).

John, T., Gussone, N., Podladchikov, Y. Y., Bebout, G. E., Dohmen, R., Halama, R., ... & Seitz, H. M. (2012). Volcanic arcs fed by rapid pulsed fluid flow through subducting slabs. Nature Geoscience, 5(7), 489-492.

Jones, K. A., & Escher, J. C. (2002). Near-isothermal decompression within a clockwise P–T evolution recorded in migmatitic mafic granulites from Clavering Ø, NE Greenland: implications for the evolution of the Caledonides. Journal of Metamorphic Geology, 20(3), 365-378.

Kato, T. T., & Godoy, E. (2015). Middle to late Triassic mélange exhumation along a pre-Andean transpressional fault system: coastal Chile (26°–42° S). International Geology Review, 57(5-8), 606-628.

Kato, T. T., Sharp, W. D., & Godoy, E. (2008). Inception of a Devonian subduction zone along the southwestern Gondwana margin: 40Ar-39Ar dating of eclogite-amphibolite assemblages in blueschist boulders from the Coastal Range of Chile (41 S). Canadian Journal of Earth Sciences, 45(3), 337-351.

Kay, S. M., Gorring, M., & Ramos, V. A. (2004). Magmatic sources, setting and causes of Eocene to Recent Patagonian plateau magmatism (36 S to 52 S latitude). Revista de la Asociación Geológica Argentina, 59(4), 556-568.

Kimura, J. I., Stern, R. J., & Yoshida, T. (2005). Reinitiation of subduction and magmatic responses in SW Japan during Neogene time. Geological Society of America Bulletin, 117(7-8), 969-986.

Kohn, M. J., Spear, F. S., Harrison, T. M., Dalziel, I. W. D. (1995). 40Ar/39Ar geochronology and P-T-t paths from the Cordillera Darwin metamorphic complex, Tierra del Fuego. Chile. Journal of Metamorphic Geology, 13, 251-270.

Kohn, M. J., Corrie, S. L., Markley, C. (2015). The fall and rise of metamorphic zircon. American Mineralogist, 100, 897-908.

Kohn, M. J., & Spear, F. S. (1990). Two new geobarometers for garnet amphibolites, with applications to southeastern Vermont. American Mineralogist, 75(1-2), 89-96.

Lázaro, C., & García-Casco, A. (2008). Geochemical and Sr–Nd isotope signatures of pristine slab melts and their residues (Sierra del Convento mélange, eastern Cuba). Chemical Geology, 255(1), 120-133.

Ludwig, K. R. (2009). Isoplot 4.1. A geochronological toolkit for Microsoft Excel. Berkeley Geochronology Center Special Publication, 4, 76.

Maloney, K. T., Clarke, G. L., Klepeis, K. A., Fanning, C. M., & Wang, W. (2011). Crustal growth during back-arc closure: Cretaceous exhumation history of Cordillera Darwin, southern Patagonia. Journal of Metamorphic Geology, 29(6), 649-672.

Maruyama, S., Hasegawa, A., Santosh, M., Kogiso, T., Omori, S., Nakamura, H., ... & Zhao, D. (2009). The dynamics of big mantle wedge, magma factory, and metamorphic–metasomatic factory in subduction zones. Gondwana Research, 16(3), 414-430.

Martin, H., Smithies, R. H., Rapp, R., Moyen, J. F., & Champion, D. (2005). An overview of adakite, tonalite–trondhjemite–granodiorite (TTG), and sanukitoid: relationships and some implications for crustal evolution. Lithos, 79(1), 1-24.

Mpodozis, C., & Ramos, V. A. (2008). Tectónica jurásica en Argentina y Chile: extensión, subducción oblicua, rifting, deriva y colisiones. Revista de la Asociación geológica Argentina, 63(4), 481-497.

Mukasa, S. B., & Dalziel, I. W. (1996). Southernmost Andes and South Georgia Island, North Scotia Ridge: zircon U-Pb and muscovite 40Ar39Ar age constraints on tectonic evolution of Southwestern Gondwanaland. Journal of South American Earth Sciences, 9(5), 349-365.

Nikolaeva, K., Gerya, T. V., & Marques, F. O. (2010). Subduction initiation at passive margins: numerical modeling. Journal of Geophysical Research: Solid Earth, 115(B3).

O'brien, P. J., & Rötzler, J. (2003). High-pressure granulites: formation, recovery of peak conditions and implications for tectonics. Journal of Metamorphic Geology, 21(1), 3-20.

O'Connor, J. T. (1965). A classification for quartz-rich igneous rocks based on feldspar ratios. US Geological Survey Professional Paper B, 525, 79-84.

Olivares, B., Cembrano, J., Hervé, F., López, G., and Prior, D., (2003). Geometria y cinemática de La Zona de Cizalle Seno Arcabuz, Andes patagônicos, Chile. Revista Geológica de Chile 30, 39-52.

Oncken, O., Asch, G., Haberland, C., Metchie, J., Sobolev, S., Stiller, M., ... & Görze, H. J. (2003). Seismic imaging of a convergent continental margin and plateau in the central Andes (Andean Continental Research Project 1996 (ANCORP'96)). Journal of Geophysical Research: Solid Earth, 108(B7).

Parada, M.A., López-Escobar, L., Oliveros, V., Fuentes, F., Morata, D. et al. (2007). Andean Magmatism. In: The Geology of Chile (T. Moreno and W. Gibson, eds.). The Geological Society of London. p. 115-146. Great Britain.


Pankhurst, R. J., Riley, T. R., Fanning, C. M., & Kelley, S. P. (2000). Episodic silicic volcanism in Patagonia and the Antarctic Peninsula: chronology of magmatism associated with the break-up of Gondwana. Journal of Petrology, 41(5), 605-625.

Pattison, D. R. M. (2003). Petrogenetic significance of orthopyroxene-free garnet+ clinopyroxene+ plagioclase±quartz-bearing metabasites with respect to the amphibolite and granulite facies. Journal of Metamorphic Geology, 21(1), 21-34.

Peacock, S. M., Rushmer, T., & Thompson, A. B. (1994). Partial melting of subducting oceanic crust. Earth and planetary science letters, 121(1), 227-244.

Peacock, S. M. (1991). Numerical simulation of subduction zone pressure-temperature-time paths: constraints on fluid production and arc magmatism. Philosophical Transactions of the Royal Society of London A: Mathematical, Physical and Engineering Sciences, 335(1638), 341-353.

Peacock, S. M., & Wang, K. (1999). Seismic consequences of warm versus cool subduction metamorphism: Examples from southwest and northeast Japan. Science, 286(5441), 937-939.

Pearce, J. A. (2008). Geochemical fingerprinting of oceanic basalts with applications to ophiolite classification and the search for Archean oceanic crust. Lithos, 100(1), 14-48.

Petford, N. (1995). Segregation of tonalitic-trondhjemitic melts in the continental crust: The mantle connection. Journal of Geophysical Research: Solid Earth, 100(B8), 15735-15743.

Plank, T., & Langmuir, C. H. (1993). Tracing trace elements from sediment input to volcanic output at subduction zones. Nature, 362(6422), 739-743.

Platt, J. P. (1986). Dynamics of orogenic wedges and the uplift of high-pressure metamorphic rocks. Geological society of America bulletin, 97(9), 1037-1053.

Powell, R., & Downes, J. (1990). Garnet porphyroblast-bearing leucosomes in metapelites: mechanisms, phase diagrams, and an example from Broken Hill, Australia. In High-temperature metamorphism and crustal anatexis (pp. 105-123). Springer Netherlands.

Powell, R., & Holland, T. (1999). Relating formulations of the thermodynamics of mineral solid solutions: activity modeling of pyroxenes, amphiboles, and micas. American Mineralogist, 84(1-2), 1-14.

Powell, R., & Holland, T. (1994). Optimal geothermometry and geobarometry. American Mineralogist, 79(1-2), 120-133.

Prouteau, G., Scaillet, B., Pichavant, M., & Maury, R. (2001). Evidence for mantle metasomatism by hydrous silicic melts derived from subducted oceanic crust. Nature, 410(6825), 197-200.

Ramos, V. A. (1994). Terranes of southern Gondwanaland and their control in the Andean structure (30–33 S latitude). In Tectonics of the Southern Central Andes (pp. 249-261). Springer Berlin Heidelberg.

Rapp, R. P., Watson, E. B., & Miller, C. F. (1991). Partial melting of amphibolite/eclogite and the origin of Archean trondhjemites and tonalites. Precambrian Research, 51(1), 1-25.

Ravna, K. (2000). The garnet–clinopyroxene $Fe^{2+}$–Mg geothermometer: an updated calibration. Journal of metamorphic Geology, 18(2), 211-219.

Rossetti, F., Nasrabady, M., Vignaroli, G., Theye, T., Gerdes, A., Razavi, M. H., & Vaziri, H. M. (2010). Early Cretaceous migmatitic mafic granulites from the Sabzevar range (NE Iran): implications for the closure of the Mesozoic peri-Tethyan oceans in central Iran. Terra Nova, 22(1), 26-34.

Rubatto, D., Hermann, J., Berger, A., & Engi, M. (2009). Protracted fluid-induced melting during Barrovian metamorphism in the Central Alps. Contributions to Mineralogy and Petrology, 158(6), 703-722.

Sawyer, E. W., 2014. The inception and growth of leucosomes: microstructure at the start of melt segregation in migmatites. Journal of Metamorphic Geology, 32, 695-712.

Schmidt, M. W., & Poli, S. (2014). 4.19. Devolatilization during subduction. The Crust, Treatise on Geochemistry (eds. HD Holland and KK Turekian, Second Edition), Elsevier-Pergamon, Oxford, 669-701.

Sepúlveda, F.A., Palma-Heldt, S., Hervé, F., Fanning, M. (2010). Permian depositional age of metaturbidites of the Duque de York Complex, Southern Chile: U-Pb SHRIMP data and palynology. Andean Geology 37, 375-397.

Shelley, D. (1967). Myrmekite and myrmekite-like intergrowths. Mineralogical Magazine, 36(280), 491-503.

Smye, A. J., Greenwood, L. V., & Holland, T. J. B. (2010). Garnet–chloritoid–kyanite assemblages: eclogite facies indicators of subduction constraints in orogenic belts. Journal of Metamorphic Geology, 28(7), 753-768.

Snoeyenbos, D. R., Williams, M. L., & Hanmer, S. (1995). Archean high-pressure metamorphism in the western Canadian Shield. European Journal of Mineralogy, 1251-1272.

Sorensen, S. S., & Barton, M. D. (1987). Metasomatism and partial melting in a subduction complex Catalina Schist, southern California. Geology, 15(2), 115-118.

Sorensen, S. S. (1988). Petrology of amphibolite-facies mafic and ultramafic rocks from the Catalina Schist, southern California: Metasomatism and migmatization in a subduction zone metamorphic setting. Journal of Metamorphic Geology, 6(4), 405-435.

Spandler, C., & Pirard, C. (2013). Element recycling from subducting slabs to arc crust: A review. Lithos, 170, 208-223.

Stern, R. J. (2004). Subduction initiation: spontaneous and induced. Earth and Planetary Science Letters, 226(3), 275-292.

Stern, C. R., & De Wit, M. J. (2003). Rocas Verdes ophiolites, southernmost South America: remnants of progressive stages of development of oceanic-type crust in a continental margin back-arc basin. Geological Society, London, Special Publications, 218(1), 665-683.

Sun, S. S., & McDonough, W. S. (1989). Chemical and isotopic systematics of oceanic basalts: implications for mantle composition and processes. Geological Society, London, Special Publications, 42(1), 313-345.

Syracuse, E. M., van Keken, P. E., & Abers, G. A. (2010). The global range of subduction zone thermal models. Physics of the Earth and Planetary Interiors, 183(1), 73-90.

Tatsumi, Y., & Eggins, S. (1995). Subduction zone magmatism (Vol. 1). Wiley. Frontiers in earth sciences. DOI: 086542361X 9780865423619.

Torres-Roldan, R. L., Garcia-Casco, A., and Garcia-Sanchez, P. A. (2000). CSpace: an integrated workplace for the graphical and algebraic analysis of phase assemblages on 32-bit Wintel platforms. Computers and Geosciences, 26(7), 779-793.

Uliana, M. A., Biddle, K. T., & Cerdan, J. (1989). Mesozoic extension and the formation of Argentine sedimentary basins. In A. J. Tankard, & H. R. Balkwill (Eds.), Extensional tectonics and stratigraphy of the North Atlantic margins (Vol. 46, pp. 599-614). Tulsa-Oklahoma, Oklahoma: American Association of Petroleum Geologists.

Van Hunen, J., & Moyen, J. F. (2012). Archean subduction: fact or fiction?. Annual Review of Earth and Planetary Sciences, 40, 195-219.

Vidal, O., Parra, T., & Trotet, F. (2001). A thermodynamic model for Fe-Mg aluminous chlorite using data from phase equilibrium experiments and natural pelitic assemblages in the 100 to 600 C, 1 to 25 kb range. American journal of Science, 301(6), 557-592.

Vielzeuf, D., & Schmidt, M. W. (2001). Melting relations in hydrous systems revisited: application to metapelites, metagreywackes and metabasalts. Contributions to Mineralogy and Petrology, 141(3), 251-267.

Villa, I. M., De Bièvre, P., Holden, N. E., & Renne, P. R. (2015). IUPAC-IUGS recommendation on the half life of 87 Rb. Geochimica et Cosmochimica Acta, 164, 382-385.

Villa, I. M. (1998). Isotopic closure. Terra Nova-Oxford, 10(1), 42-47.

Walowski, K. J., Wallace, P. J., Hauri, E. H., Wada, I., & Clynne, M. A. (2015). Slab melting beneath the Cascade Arc driven by dehydration of altered oceanic peridotite. Nature Geoscience, 8(5), 404-408.

White, R. W., Powell, R., & Holland, T. J. B. (2007). Progress relating to calculation of partial melting equilibria for metapelites. Journal of Metamorphic Geology, 25(5), 511-527.

White, R. W., Powell, R., & Holland, T. J. B. (2001). Calculation of partial melting equilibria in the system Na2O–CaO–K2O–FeO–MgO–Al2O3–SiO2–H2O (NCKFMASH). Journal of Metamorphic Geology, 19(2), 139-153.

Whitney, D. L., & Evans, B. W. (2010). Abbreviations for names of rock-forming minerals. American mineralogist, 95(1), 185.

Williams, I.S., Claesson, S., 1987. Isotopic evidence for the Precambrian provenance and Caledonian metamorphism of high grade paragneisses from the Seve Nappes, Scandinavian Caledonides. II: Ion microprobe zircon U-Th-Pb. Contribution to Mineralogy and Petrology 97, 205-217.

Willner, A. P., Pawlig, S., Massonne, H. J., and Hervé, F. (2001). Metamorphic evolution of spessartine quartzites (coticules) in the high-pressure, low-temperature complex at Bahia Mansa, Coastal Cordillera of South-Central Chile. The Canadian Mineralogist, 39(6), 1547-1569.

Willner, A. P., Glodny, J., Gerya, T. V., Godoy, E., and Massonne, H. J. (2004a). A counterclockwise PTt path of high-pressure/low-temperature rocks from the Coastal Cordillera accretionary complex of south-central Chile: constraints for the earliest stage of subduction mass flow. Lithos, 75(3), 283-310.

Willner, A. P., Hervé, F., Thomson, S. N., and Massonne, H. J. (2004b). Converging PT paths of Mesozoic HP-LT metamorphic units (Diego de Almagro Island,

Southern Chile): evidence for juxtaposition during late shortening of an active continental margin. Mineralogy and Petrology, 81(1-2), 43-84.

Willner, A. P. (2005). Pressure–temperature evolution of a Late Palaeozoic paired metamorphic belt in North–Central Chile (34–35 30′ S). Journal of Petrology, 46(9), 1805-1833.

Willner, A. P., Sepúlveda, F. A., Hervé, F., Massonne, H. J., and Sudo, M. (2009). Conditions and timing of pumpellyite–actinolite-facies metamorphism in the Early Mesozoic Frontal Accretionary Prism of the Madre de Dios Archipelago (latitude 50 20′ S; Southern Chile). Journal of Petrology, 50(11), 2127-2155.

Willner, A. P., Massonne, H. J., Ring, U., Sudo, M., & Thomson, S. N. (2012). P–T evolution and timing of a late Palaeozoic fore-arc system and its heterogeneous Mesozoic overprint in north-central Chile (latitudes 31–32 S). Geological Magazine, 149(02), 177-207.

Wolf, M. B., & Wyllie, P. J. (1993). Garnet growth during amphibolite anatexis: implications of a garnetiferous restite. The Journal of Geology, 357-373.

Yamamoto, H., & Yoshino, T. (1998). Superposition of replacements in the mafic granulites of the Jijal complex of the Kohistan arc, northern Pakistan: dehydration and rehydration within deep arc crust. Lithos, 43(4), 219-234.

Zen, E. A., & Hammarstrom, J. M. (1984). Magmatic epidote and its petrologic significance. Geology, 12(9), 515-518.

**Table 1**: Representative minerals analyses for both stage 1 (HT) and stage 2 parageneses (LT).

**Table 2**: Bulk-rock compositions of studied samples from the Lazaro unit. (*): analysis made in ACMElabs, Canada. (**): analysis made in GFZ Potsdam, Germany.

**Table 3**: Thermobarometric results on Lazaro unit garnet amphibolites and granulite-facies rocks using the calibrations of [1] Kohn and Spear (1990), [2] Ravna (2000) and [3] Ellis and Green (1979). Average P calculations have been made following Powell & Holland (1994).

**Electronic Appendix 1**: Field and BSE images of studied rocks.

1682 **Electronic Appendix 2**: Microstructure of sample #29a and details of Chl-Phg

1683 thermobarometric estimates.

1684 **Electronic Appendix 3**: Rb-Sr and Sm-Nd isotopic data.

1685 **Electronic Appendix 4**: U-Th-Pb SHRIMP data for the metasedimentary sample

1686 #24: d (%) = 100 ×(1 - 206/238 age / 207/235 age); $f^{206}$ % = (common $^{206}$Pb / total

1687 $^{206}$Pb) × 100. All errors are at 95% confidence level.

1688 **Electronic Appendix 5**: Thermo-kinematic numerical model result showing the

1689 thermal structure of a young subduction zone 4 Ma after initiation.